LIMNOLOGY
and
OCEANOGRAPHY: METHODS

ASLO

Limnol. Oceanogr.: Methods 17, 2019, 585–606

doi: 10.1002/lom3.10335

Laboratory and field investigations on freeze and gravity core sampling and assessment of coring disturbances with implications on gas bubble characterization[a]

Yannick Dück,[1]* **Andreas Lorke**,[2] **Christian Jokiel**,[1] **Johannes Gierse**[1]

[1]Institute of Hydraulic Engineering and Water Resources Management, Cologne University of Applied Sciences, Cologne, Germany

[2]Institute for Environmental Sciences, University of Koblenz-Landau, Landau, Germany

Abstract

The quantification of greenhouse gas emissions from aquatic ecosystems requires knowledge about the spatial and temporal dynamics of free gas in sediments. Freezing the sediment in situ offers a promising method for obtaining gas-bearing sediment samples, unaffected by changes in hydrostatic pressure and sample temperature during core withdrawal and subsequent analysis. This article presents a novel freeze coring technique to preserve the in situ stratigraphy and gas bubble characteristics. Nondestructive X-ray computed tomography (CT) scans were used to identify and characterize coring disturbances of gravity and freeze cores associated with gassy sediment, as well as the effect of the freezing process on the gas bubble characteristics. Real-time X-ray CT scans were conducted to visualize the progression of the freezing process. Additional experiments were conducted to determine the freezing rate to assess the probability of sediment particle/bubble migration, and gas bubble nucleation at the phase transition of pore water to ice. The performance of the freeze coring technique was evaluated under field conditions in Olsberg and Urft Reservoir (Germany). The results demonstrate the capability of the freeze coring technique for the preservation of gas-bearing sediments and the analysis of gas bubble distribution pattern in both reservoirs. Nevertheless, the obtained cores showed that nearly all gravity and freeze cores show some degree of coring disturbances.

The ability to collect sediment samples from aquatic ecosystems that retain the in situ sedimentological properties is a fundamental prerequisite in various research and engineering fields, for example, for the accurate quantification of sedimentation rates, organic matter (OM) mineralization rates, gas fluxes, and determination of contaminated sediment layers. Consequently, it is necessary to preserve both the sediment structural integrity and ambient (in situ) conditions. Many authors have questioned the validity of results obtained from ex situ sediment analyses because of the sampling bias associated with the coring device used (Baxter et al. 1981; Blomqvist 1985; Buckley et al. 1994). The lack of validation studies for sediment coring techniques in shallow coastal environments has generated assumptions as the legitimacy of employing ex situ analyses on samples obtained in this way (Mogg et al. 2017).

In recent years, aquatic ecosystems (e.g., lakes, reservoirs, rivers, and coastal waters) have been recognized as an important source of the potent greenhouse gas methane (CH_4) (Bastviken et al. 2011). CH_4 is formed in aquatic sediment through anaerobic decomposition of OM (Martens and Berner 1974), and can be stored and released as gas bubbles. Ebullition-mediated flux is often highly variable in space and time (Varadharajan and Hemond 2012; Maeck et al. 2014; Wilkinson et al. 2015), with sediment gas storage being an important parameter for explaining these dynamics (Liu et al. 2016). In addition, experiments demonstrated that gas formation and transport in sediments can be described as a function of gas bubble shape, orientation, and size distributions (Boudreau et al. 2005; Algar et al. 2011; Liu et al. 2016). To apply these experimental and theoretical findings, in situ sediment gas content and bubble size distribution need to be analyzed and validated with in situ sediment cores.

*Correspondence: yannick.dueck@posteo.de

[a]**Author Contribution Statement:** Y.D. is responsible for the study design, data analysis, and text. A.L. and C.J. support the entire process. J.G. support the data analysis.

Additional Supporting Information may be found in the online version of this article.

The widespread demand for sediment coring has resulted in the development of a large variety of different sampling techniques in the last decades. Comparative assessments of coring techniques and how well they preserve the in situ conditions are limited of soft-bottom sediments (e.g., Blomqvist 1991; Chant and Cornett 1991; Environmental Protection Agency 1991; Jutzeler et al. 2014). Those studies showed that sediment core sampling techniques, extraction, transport storage, and specimen transportation are subject to various types of coring disturbances and therefore may not always represent the in situ sediment characteristics.

There is a special problem associated sampling of with gas-bearing sediment due to the change in hydrostatic pressure and sample temperature upon the sediment sample brought to the surface from a depth of several meters. The formation of free gas can occur over a few hours after the cores were taken due to the rise in temperature (the lake bottom is usually colder than the temperature at the surface of the lake or in the transportation vehicle), causing reduction in methane solubility (Lane and Taffs 2002) and resulting in an increase in gas production. None of traditional tube coring techniques (e.g., gravity or vibra corers) can take intact cores without causing significant disturbances to gas-bearing sediment and they are not applicable for collecting water-saturated sediment, if cohesion is low where the sample liquefies and can be lost during core recovery (Strasser et al. 2015).

The drawback of depressurization can be avoided by preserving in situ hydrostatic pressure. Pressure corers have been developed for characterizing gas-bearing sediment in Eckernförde Bay, Germany (Abegg and Anderson 1997). The in situ hydrostatic pressure was preserved by capping a pressure tight aluminum transfer chamber on the seabed floor with the help of divers. However, the application of pressure cores obtained by divers is limited to shallow depths (Abegg and Anderson 1997). Various pressure corers have been developed and deployed in marine environments, such as the Pressure Coring Barrel developed by the Deep Sea Drilling Project and the Pressure Coring Sampler developed by the Ocean Drilling Program (Li et al. 2016). Such pressure corer requires expertise and a proper platform to operate, which makes sampling complex and expensive.

As an alternative technique, freeze coring has been introduced to take sediment cores for the collection and detailed stratigraphic analysis, even if they have a low cohesion (Lisle 1989). When taking freeze cores, sediment is frozen to the surface of the sampler, which is filled with a coolant such as dry ice (preferably mixed with ethanol) or liquid nitrogen (Pachur et al. 1984). In principle, this preserves sediment gas bubbles in frozen cores under in situ hydrostatic pressure and therefore prevents the sudden degassing of bubbles (Verschuren 2000). To our knowledge, no previous research has investigated the possibility of freeze coring for obtaining gas-bearing sediment and the determination of the different types and extent of coring disturbances between in situ frozen and unfrozen sediment samples for gas bubble analysis. However, even though freeze coring has been introduced as an alternative method for taking gas-bearing sediment cores, most of the previous studies did not investigate the effect of the freezing process on the sediment sample. Little is known about how and to what extent the structural integrity of the sediment, the gas content, and bubble distribution is affected by freezing. Most of the theories and studies on the physical effects of freezing are focused on soil and pure water which may only be transferable to a limited extent to water-saturated or gassy sediments. Major conceptual frameworks were provided by Halde (1980) and Vesilind and Martel (1990), who reported that a slow freezing rate rejects particle by the moving ice-water interface, whereas a high freezing rate traps particle into the developing ice layer. Carte (1961) showed that air bubbles in ice could form from air originally dissolved in water before freezing.

In this article, we analyzed X-ray computed tomography (CT) scan images, which offers the possibility of a wide range of geological investigations and provides nondestructive three-dimensional (3D) visualization and characterization (Ketcham and Carlson 2001) of coring disturbances and gas bubbles. Additionally, for the first time, spectral X-ray CT scans of freeze core samples were conducted, which allowed us to determine the effective atomic number (Z_{eff}) of each voxel within the core. Given that in situ stratigraphy dimensions are generally unavailable for comparison of recovered cores, comparative laboratory experiments of freeze and gravity cores with different sediment parameters, stratigraphy, and constant/inconstant penetration velocity were conducted. The experiments additionally included the measurement of the freezing rate and real-time CT scans to examine the freezing process of this coring technique with sediments, differing in grain size distribution (GSD), water content (WC), and OM. Field investigations were conducted to test the applicability and suitability of the freeze corer to characterize gas bubbles, and to determine the coring disturbances in comparison to those obtained in the laboratory studies.

This article aims to provide more thorough documentation of the causes, effects, and extents of physical coring disturbances of a novel freeze coring technique, and to introduce certain disturbed structures that are rarely previously described in the literature. We first review different types of coring disturbances, before we describe the methods used for laboratory and field investigations. Examples of coring disturbances are given from selected laboratory and field cores. In particular, we focus on coring disturbances due to the freezing process of the sediment in situ and on the analysis of gas bubbles characteristics. Finally, we illustrate and discuss the scientific importance of the identification of coring disturbances, and we outline guidelines for the appropriate use of freeze or gravity corer under specific boundary conditions.

Coring disturbances

In this section, we briefly review the most common causes and effects of coring disturbances, from descending the corer

to the sediment surface to the handling of the core in the laboratory (Fig. 1).

Shock wave

The corer can create a hydraulic shock wave (bow wave) in front of the orifice of the cutting-edge when the unimpeded water flow through the corer is restricted (Fig. 1a). This shock wave can wash away fluffy surficial sediment before the corer reaches the sediment–water interface. This source of error has been reported for open barrel gravity corers (McIntyre 1971; Elmgren 1973; Baxter et al. 1981; Jensen 1983; Leonard 1990) and piston corers (McCoy and von Herzen 1971; McCoy 1972; Stowe and Aksu 1978; McCoy 1980). Unimpeded water flow through the corer during descent and a careful lowering to the last few centimeters to minimize the dispersion of fine material due to a sample-induced shock wave is required (McIntyre 1971; Glew et al. 2001; Taft and Jones 2001).

Penetration disturbance

Vibra coring uses (Fig. 1b) high frequency–low amplitude corer vibration that liquefies a thin layer of water-saturated sediment at the core tube that leading to a loss of sediment strengths and eases penetration (Glew et al. 2001). It is preferred for fine-grained sediment like sand, silt, and clay with average core compaction of over 40% (Smith 1992, 1998).

Gravity corers are inserted into the sediment using a hammering method (Fig. 1b), whereby a ram or hydrostatic motor is used to lift and release a weight to hammer the corer into

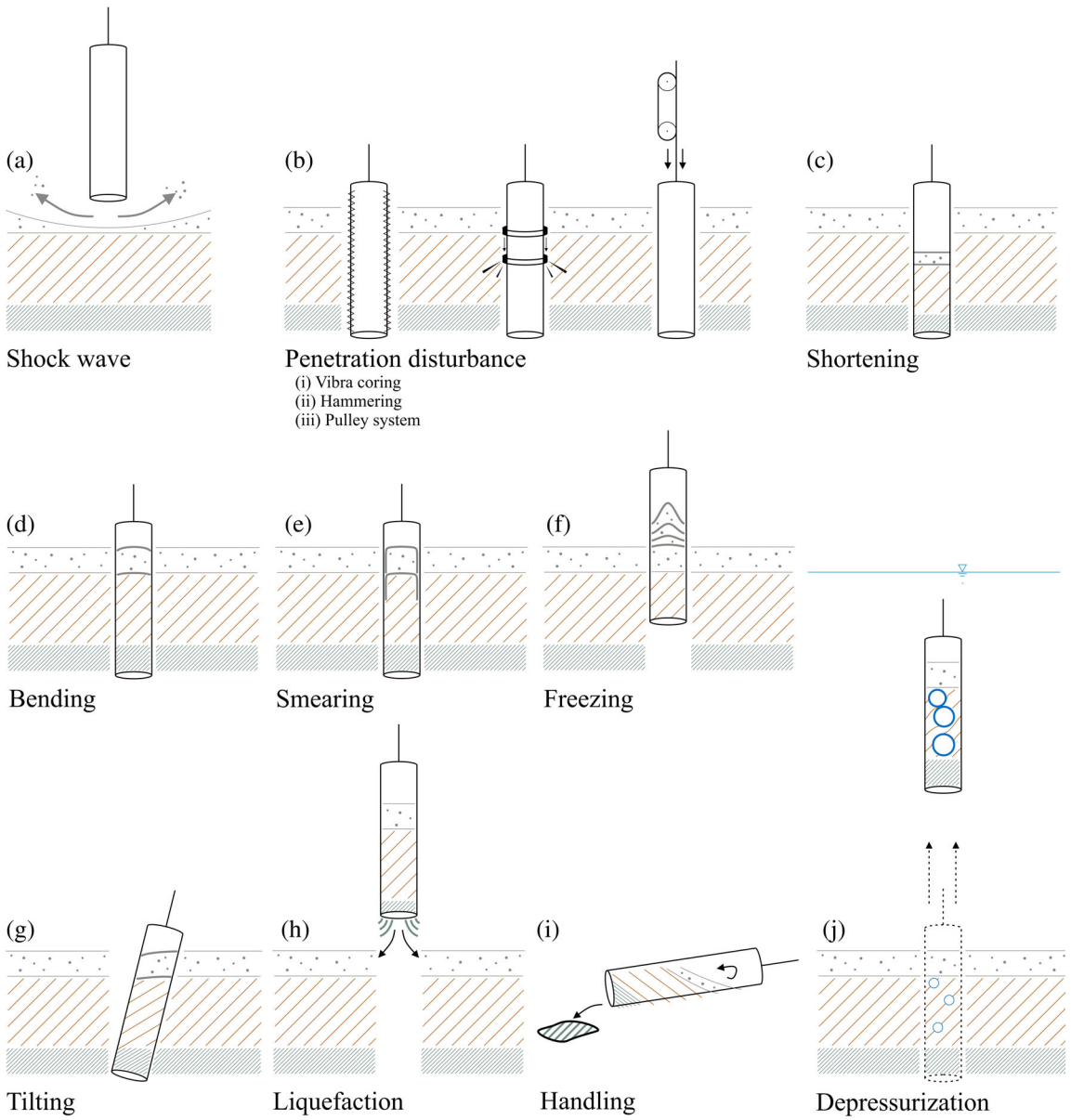

Fig. 1. Schematic presentation of typical coring disturbances. The explanation of the individual coring disturbances can be found in chapter 2.

the sediment (Wang et al. 2011). Core shortening is a known problem of this method and its impact varies with the penetration velocity and sediment type (Parker and Sills 1989).

By pulling a rope attached to the supporting stand (tripod) of the corer, the corer is constantly pulled into the sediment (Fig. 1b). By using a tripod, the penetration velocity can be adjusted, since a slow penetration velocity reduces sediment deformation and compaction (Martin and Miller 1982; Wright 1993; Lane and Taffs 2002).

Shortening

Shortening is the reduction of the sediment core length compared to the actual length (Skinner and McCave 2003) by physical compaction, sediment thinning, sediment bypassing (Morton and White 1997), and/or partial loss of the sample during withdrawal of the corer from the sediment (Fig. 1c). Core shortening occurs mainly due to friction between the sediment and inner tube wall of the corer. The pressure in the corer and the inner wall friction rises, as the sediment gradually becomes more compact. When the internal resistance of the sediment inside the core is equal to the force of the sediment being penetrated, the sediment in front of the corer is forced aside and no material enters the tube. The corer begins to act partly as a plow and core shortening begins. It is also possible that the plow force results in a down bending and stretching of layers, until they are finally cut, and the sediment enters the corer. Therefore, the effect of core compression must be extended by the possibility that sediment is pushed out of the way due to sampling resistance based on a high pressure inside the corer (Glew et al. 2001). Shortening typically occurs, if soft sediment is overlaid by stiffer matter, however, the former is more thinned than the latter (e.g., Piggot 1941; Hvorslev 1949; Hongve and Erlandsen 1979; Weaver and Schultheiss 1983). The soft sediments are driven aside as the core barrel containing high-density sediment penetrates deeper (Morton and White 1997). Clayey and silty sediments are compressed more than light, unconsolidated, organic sediments and a large core diameter minimizes shortening (Blomqvist 1991; Chaney and Almagor 2015).

Core shortening results in an altered representation of the sediment layers (Piggot 1941; Weaver and Schultheiss 1983; Blomqvist 1985). Studies have shown that core shortening patterns can be uniform (Emery and Dietz 1941; Richards and Keller 1961; Emery and Hülsemann 1964; Lebel et al. 1982), progressive over depth (Richards and Keller 1961; Weaver and Schultheiss 1983), or a mixture of different patterns (Parker and Sills 1989).

The subsequent analysis of sediment core data requires an adjustment of the core stratigraphy to remove the effects of shortening with respect to their natural position in order to avoid any over- or underestimation. This coring disturbance produces a bias in samples, which is difficult to detect (Kallstenius 1958) and may severely bias the sampling (Emery and Dietz 1941; Piggot 1941; Hvorslev 1949; Richards and Keller 1961; Emery and Hülsemann 1964; Hongve and Erlandsen 1979; Lebel et al. 1982; Weaver and Schultheiss 1983; Blomqvist 1985, 1991). For example, sedimentation rates calculated from shortened cores maybe two to three times lower than rates calculated from unshortened cores (Nevissi et al. 1989; Crusius and Anderson 1991).

Bending

Bending is the result of coring-induced shear between the sediment and the corer (Skinner and McCave 2003) and/or the force of the partly filled corer, which is down-bending sediment layers (Fig. 1d) ahead of the end of the cutting-edge as it penetrates the sediment (Emery and Dietz 1941). Kegwin et al. (1998) described this effect as a function of core barrel radius and degree of deformation. Bending can be recognized as downward dredging of a layer near to the core liner and the sediment.

Smearing

Smearing is the frictional downward dragging of overlying sediment material along the core tube wall into deeper layers (Fig. 1e). It can occur when the tube penetrates the sediments and/or when the core is extruded from the core liner during sectioning in the lab. The risk of smearing increases with decreasing tube diameters (Nies et al. 1990).

Smearing may change the depth gradients of materials in the core from those present under in situ conditions (Chant and Cornett 1991), and, particularly in studies dealing with trace components, might also create a contamination problem (e.g., Stowe and Aksu 1978; Harvey et al. 1987; Chant and Cornett 1991; Jutzeler et al. 2014). Smearing can be recognized as a smear of sediment along the inside of and near to the core barrel, whereas the flowage along the core liner is likely over long sections of the core.

Freezing

The sediment is being subjected to changes in physical properties, like density, pore space, shear strength, thermal properties, and chemical properties of the particles and pore water due to the freezing process (Fig. 1f). The majority of those effects are described in the literature for soil freezing under natural conditions or sludge freeze for the dewatering in the process industry. Due to this lack in literature, those phenomenon needs to be transferred, as far as the results are transferable, to sediment freezing.

During the phase transition, the density of water decreases rapidly, and the volume expands by about 9%. It is followed by a continuous decrease of volume until the sample achieves −70°C; below this temperature, all sediments are frozen (Tsytovich 1975). Rutledge and Fleeger (1988) have shown a distortion of the vertical stratigraphy, whereas the extent and shape of distortion depend on the freezing rate, which is related to the chosen coolant. This effect can accumulate to a certain extent in vertical direction. Besides the freezing rate, it

can be reasonably assumed that the vertical distortion of the sediment layer depends on various ambient conditions (e.g., hydrostatic pressure, water temperature, etc.) and sediment characteristics (WC, OM, GSD, etc.).

The ice crystal formation can be accomplished with the separation of particles and/or gas bubbles. Due to the compressibility and temperature-dependent volume change of gases, the gas volume can also change during the freezing process. Furthermore, Carte (1961) observed the nucleation and entrapment of gas bubbles by an advancing ice-water interface, since gas solubility in ice is at least two orders of magnitude smaller than in water (Killawee et al. 1998). Therefore, bubbles may form due to nucleation at the water-ice boundary when the water at the interface becomes supersaturated. Bubble concentration and sizes were found to be depending on the rate of freezing (Carte 1961).

Tilting

When the corer hits the lake-bed, vessel movement may tilt the corer (Fig. 1g) and result in redistribution and resuspension of enclosed sediment as well as the loss of material (Blomqvist 1985, 1991). The sampler also may sink deeper into the sediment than its length and over-penetrate the sediment (e.g., Flannagan 1970; Blomqvist 1991). Therefore, a supporting stand, favorable weather conditions, high ship stability, and anchoring before sampling reduce the probability of this disturbance type.

Liquefaction/deformation due to core recovery and transport on deck

Conventional sampling techniques to extract water-saturated sands, as well as unconsolidated silts and clays fail, if the cohesion of the sediment is low, resulting in a (partial) liquefaction of the sample (Fig. 1h) (Schreiner and Kreysing 2013; Jutzeler et al. 2014; Strasser et al. 2015). During corer recovery, the sample is exposed to pressure variations due to suction, while pulling the corer out of the sediment and decreasing pressure while lifting the corer to the water surface (Blomqvist 1985). An acceleration of the corer may result in a resuspension leading to (partial) leaking out of the sample (Blomqvist 1991). Even a small amount of gas may cause large dissipation rates and increase the risk of momentary liquefaction in the soil considerably (Sumer and Fredsøe 2002).

Sample handling

When the sediment core is pushed out of the corer for subsample processing, the sediment may be disturbed by forces and friction during extrusion and moisture changes (Fig. 1i) (Hopper 1992). The force required to extrude the sample from the sampling tube is larger than the unconfined strength of clayey silt (e.g., Arman and MacManis 1976; Jutzeler et al. 2014), which can result in smearing or bending of the sediment layer. Tumbling and horizontal storage of the core on deck may also increase disturbances in the sample (e.g., mixing).

Depressurization/change in temperature

The sediment core structure obtained with nonpressurized sampling techniques can be deformed by gas bubble expansion and ebullition upon lifting the corer through the water column (Fig. 1j) (Wright 1993; Scandella et al. 2011). The change in hydrostatic pressure and sample temperature on the sediment sample being brought from the lake-bed to the surface causes a dissolution of gases, causes the formation of gas bubbles which rose to the top of the core and destroying the stratigraphy (Rymer and Neale 1981; Lane and Taffs 2002). Even hours after the core arrives was retrieved, an increase in gas production, expansion, and subsequent escape of gas from sediment can occur (Flood et al. 1995). Wever et al. (1998) demonstrated that sediment gas content can increase by six times in half an hour after 0.5 bar pressure release. A number of authors have recognized that gas bubble migration destroys the stratigraphy (Förstner et al. 1968) or postulated that degassing after core retrieval result in elongated fissures and vertical cracks (Schubel 1974; Milkert 1993). Freezing the sample may be the only way to overtime those in situ disturbances (Rymer and Neale 1981).

Methods

Corer design

This study was performed in two phases: a laboratory phase, which focused on the identification of the causes, types, and extents of coring disturbances, and a field phase which focused on the feasibility and applicability of the freeze coring technique with an emphasis on sampling and characterization of gas-bearing and water-saturated sediment. Both, the laboratory experiments and field investigations were conducted with the novel, custom made freeze corer with a tripod and a gravity corer with hammering action (UWITEC, Austria) (Fig. 2).

The newly designed freeze corer (Fig. 2) is a further development of the remote-controlled freeze corer described by Lotter et al. (1997). For a detailed description of the new corer design, see Dück et al. (2019). The tripod is made of modular low-weight aluminum, which can easily be assembled and extended. All components can be transported in two cases with a total weight of 40 kg. The three bars, with stabilizing crossbars, have a length of 50 cm. The tripod is loosely tethered to a boat and unaffected by vessel motion to avoid disturbances before the corer actually enters the sediment (Hessler and Jumars 1974; Snider et al. 1984). Round plates with a diameter of 30 cm are mounted at the bottom of the tripod to prevent an overpenetration and tilting, which may cause disturbances (Flannagan 1970; Blomqvist 1991).

The corer is filled with the coolant and attached to the tripod. The tripod is lowered by a static rope into the water. To obtain the optimum position above the sediment surface and to avoid destroying the sediment structure, a low-cost underwater video camera (GoPro 4 Black: up to 4K/30 fps; waterproofed up to 40 m water depth) and an illumination system is mounted on the tripod. A coaxial cable transmits the WiFi signal under water

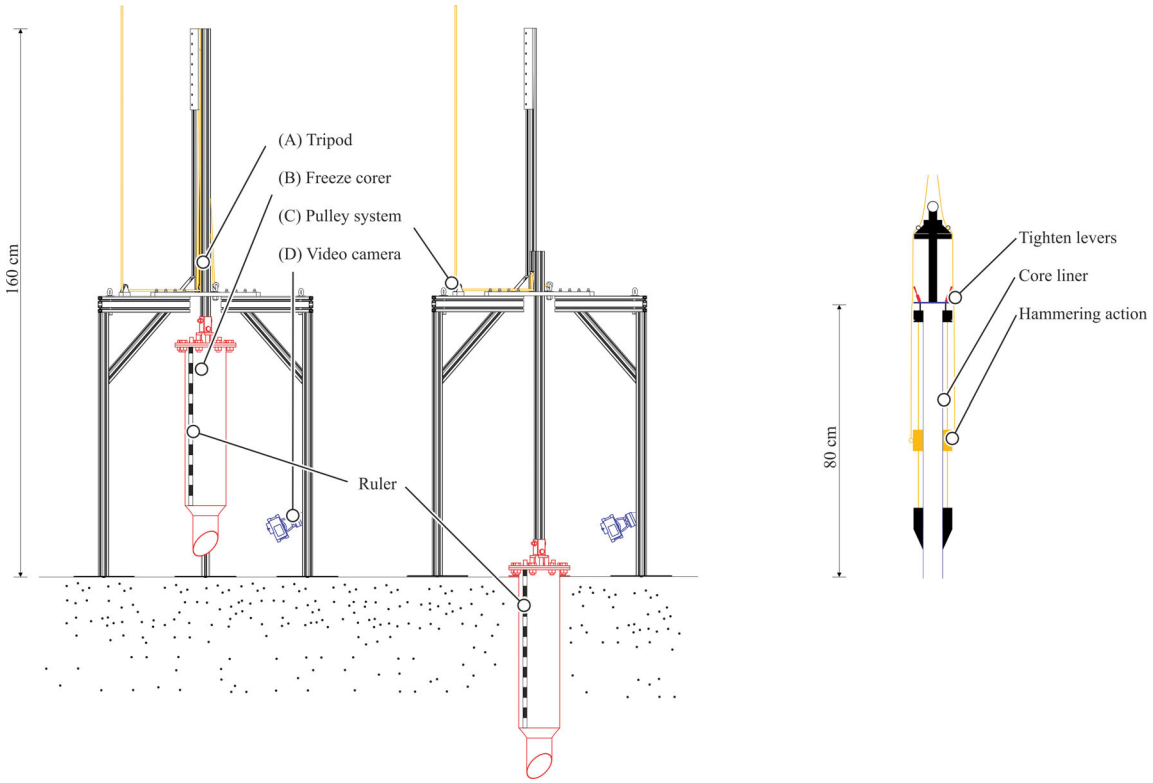

Fig. 2. Left: Sketch of the tripod and the attached freeze corer with position before and after the penetration. The device consists of four main components: (A) tripod as a supporting frame, (B) freeze corer, (C) pulley system, and (D) underwater video camera. The corer mainly consists of a (1) cutting edge, (2) a double-walled tube, and a (3) corer head. (1) Cutting edge: To reduce the penetration resistance, the lower end of the corer was beveled to a 45° angle edge (inner diameter 72 mm, length 75 mm). Above the cutting edge, the tube outer diameter increases gradually from 76 to 100 mm to reduce the penetration force. The sharp cutting-edge of 0.1 mm with an edge angle of 45° facilitates a smoother penetration of the freeze corer in contrast to the gravity corer with 1.8 mm wall thickness and a tip edge angle of 45°. (2) Double-walled tube: The double-walled tube is the container for the coolant, made of 2 mm thick stainless steel, and starts 75 mm above the cutting edge. Commercially available dry ice pellets (3 mm) and ethanol was used as coolant (temperature of approximately −78°C). The sediment core length can be up to 80 cm. The 72 mm inner diameter was chosen to allow the best ratio between minimal wall friction and short freezing time (< 30 min, which was determined in this study). (3) Corer head: The corer head is a massive stainless steel flange. It is equipped with two overpressure valves and a junction to connect the corer to the tripod. The two overpressure valves mounted on the lid of the corer allow the release of gas formed during the sublimation of the dry ice. Right: Gravity corer (Source: Uwitec) consists of a PVC core liner (80 cm long; 59 mm inner diameter) with hammering action. The penetration is controlled by its gravity and can be enhanced by hammering the corer with an attached weight into the sediment.

for real-time video transmission on board of the boat. The video monitoring also allows the measurement of the penetration depth to determine the core shortening. It also allows the observation of gas bubbles release during penetration that may bias the determination of the total gas content. After deployment on the sediment surface, the corer is slowly lowered into the sediment by pulling an additional static rope. With a four-way pulley system, a transmission ratio of 1:4 is achieved and a precise penetration process can be facilitated. With this, a hydraulic shock wave induced by penetration process can be minimized and the risk of core shortening is reduced (Blomqvist 1991).

Laboratory experiments

Coring disturbances

Comparative laboratory experiments of the freeze and gravity corer were conducted to qualitatively and quantitatively evaluate coring disturbances under controlled conditions, where the initial sediment stratigraphy is known. Four types of homogenized sediments were used, differing in predominant GSD, OM, and WC (Sand: D_{50} = 325 μm, OM: 0.0%, WC: 24.8%; Silt: D_{50} = 17 μm, OM: 2.4%, WC: 30.0%, and in situ sediment [*see* "Field investigations" section]: Olsberg: D_{50} = 65 μm, OM: 15.1%, WC: 65.0%; Urft: D_{50} = 43 μm, OM: 13.6%, WC: 63.0%). Therefore, sediment was homogenized, filled into a common springform pan (inner diameter of 30 cm) and immediately frozen with dry ice and ethanol to prevent particles from settling down during the freezing process. The frozen sediment samples were stacked in the acrylic tube (Fig. 3) with an inner diameter of 30 cm and a height of 100 cm. The sediment layers were separated by thin (~ 1 mm) layers of fluorescent pigments (Components: Phosphorescent Pigment, Zinc sulfide, copper chloride-doped; D_{50} = 21 μm; ρ = 4100 kg m^{-3}) in different colors to allow the subsequent assignment of the specific layers during the analysis. The

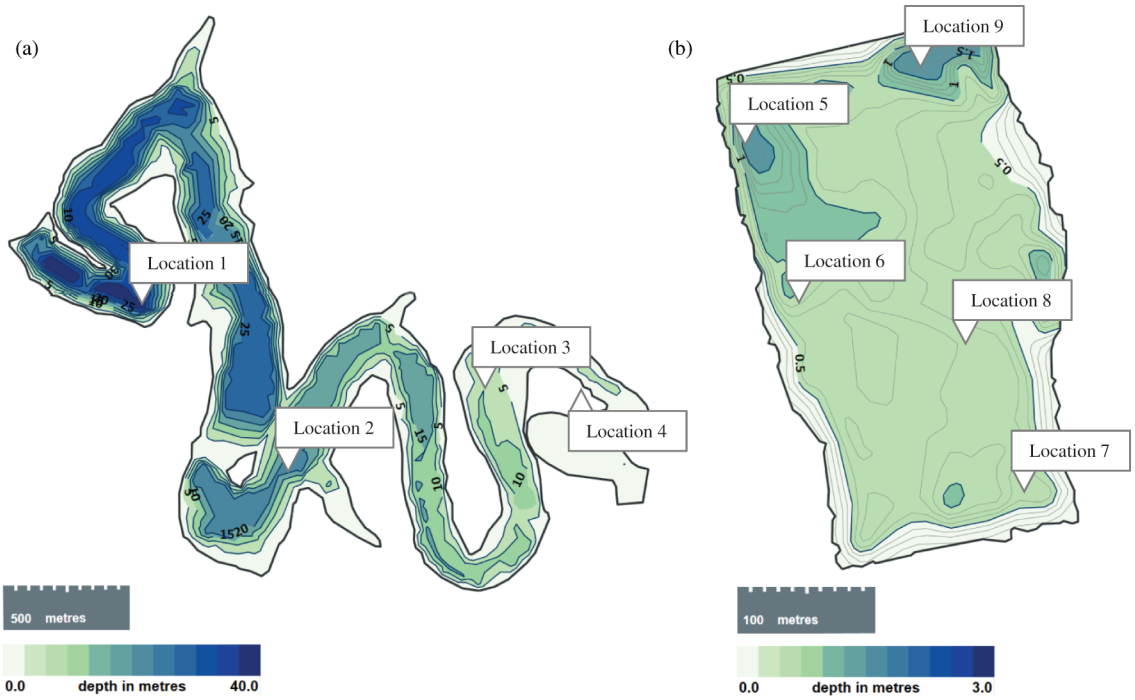

Fig. 3. Bathymetry of Urft (**a**) and Olsberg (**b**) reservoir. The sampling locations are marked on the map. The nomenclature for the field cores is for example: *Urft_GC1(frozen)_Hammering_0* is the nomenclature for *Gravity Core* (which has been frozen after the core was retrieved on deck), Sampling location *1*, *Hammering* was used for the penetration process, and no ice crust exists (0 mm).

quantity of pigments was adequate to ensure a minimum influence on the mechanical properties of the sediment. After the sediment layers were stacked, the height of each layer was documented. The samples were thawed at room temperature (~ 20°C) and the height of each layer was measured again to quantify settlements.

Twelve sets of duplicate experiments—to ensure reproducible results—with different sediment characteristics (GSD, WC, and OM), constant/inconstant penetration velocity, and with/without ice crust inside the freeze corer (an ice crust is usually formed while the corer is lowered through the water column to the sediment surface) were conducted. A constant penetration velocity (10 cm s^{-1}) was attained by using an electrical lift truck, even though the penetration force increases with penetration depth due to increased friction. An inconstant penetration velocity (~ 0.6–0.12 cm s^{-1}) was facilitated by using the tripod (as used in the field investigations). Since the penetration velocity of the gravity corer cannot be controlled in situ, it was not varied in the laboratory tests. The specifications of each experiment are summarized in Table 1. To exclude, that the diameter of the acrylic tube had an influence on the results, we conducted a preliminary examination (Set 0: *FC5_Silt_Tripod_0*; e.g., *FC5_Silt_Tripod_0* is the nomenclature for *Freeze Corer*, Experiment No. 5, *Silt Sediment*, *Tripod* as inconstant penetration velocity and an ice crust of 0 mm), with a diameter of 50 cm. The preliminary examination has revealed that the diameter has no effect on coring disturbances.

Freezing rate

Freezing rate experiments were conducted for practical reasons, to determine the time period needed for complete freezing of the sediment in field applications. Furthermore, the freezing rate can give some indication on whether the freezing process may result in particle and bubble migration, as well as bubble nucleation. Freezing rate is defined as the speed at which the water-ice interface migrates radially through the sediment column (°C min^{-1}). For the experiments, artificially sediments (*Silt* and *Sand Sediment*) and sediments taken from two reservoirs (*Olsberg* and *Urft Sediment*) were used. Additionally, tap water was tested and served as a reference sample. Duplicates of each experiment were done, to ensure reproducible results. Sediment were filled into a double-walled stainless steel tube with the freeze corer's dimensions. Sediment temperature was measured and logged with a temperature immersion sensor (Voltcraft DL-141 TH2k temperature logger, measuring range: −100°C to 1000°C; accuracy: 1°C), in the center and half the radius (R1/2) between the center of the core and the tube wall. All experiments started at ambient room temperature of approximately 20°C.

Real-time CT scans

Real-time CT scans (Philips IQon-Spectral CT, 120 kV; voxel dimension 0.126 mm^3) have been conducted to visualize the effect of freezing on the sediment structure (e.g., expansion of water, sediment particle, and bubble migration). Real-time CT scans were obtained at a 10 s time interval. Samples were filled

Table 1. Main specifications of the laboratory experiments. D_{50} denotes the median grain diameter, FC refer to freezer corer, and GC to gravity corer. Set 0 is the preliminary experiment.

ID	No. of experiments	Corer type	Sediment	D_{50} (μm)	Water content (%)	Organic matter (%)	Penetration velocity (cm s^{-1})	Sample diameter (cm)	Average shortening (%)
Set 0	1	FC	Silt	17	25.5	2.4	0.10	50	21
Set 1	4	FC	Silt	17	28.3 ± 0.4	2.4	0.10	30	6
Set 2	3	GC	Silt	17	26.8 ± 1.6	2.4	0.10	30	30
Set 4	3	FC	Silt	17	27.6 ± 2.5	2.4	0.11	30	3
Set 5	2	FC	Silt	17	28.6 ± 0.1	2.4	0.11	30	24
Set 6	2	FC	Silt/sand	17/325	27.0 ± 0.4	2.4	0.10	30	3
Set 7	2	FC	Silt/sand	17/325	29.0 ± 0.4	2.4	0.09	30	11
Set 8	2	FC	Silt/sand	17/325	27.8 ± 0.9	2.4	0.12	30	8
Set 9	2	GC	Silt/sand	17/325	26.6 ± 1.1	2.4	0.10	30	22
Set 10	2	FC	Olsberg	17	65.4 ± 0.3	14.2	0.10	30	38
Set 11	2	FC	Olsberg	17	69.1 ± 0.1	14.2	0.12	30	45
Set 12	2	FC	Olsberg	17	63.0 ± 1.8	14.2	0.06	30	3
Set 13	2	GC	Olsberg	17	66.7 ± 0.6	14.2	0.10	30	37

in graphite tubes (height: 250 mm; inner diameter: 75 mm; thickness: 2 mm) with similar dimensions of the freeze corer, surrounded by a coolant of dry ice pellets (3 mm) and ethanol. Graphite tubes (thermal conductivity $\lambda_{\text{graphite tube}}$ = 119–165 W m^{-1} K^{-1}) were used, since metallic materials (λ_{metal} = 15–58 W m^{-1} K^{-1}) cause severe artifacts in X-ray CT scans. Plastic material (λ_{plastic} = < 0.5 W m^{-1} K^{-1}) could not be used, as the thermal conductivity is significantly smaller than of the freeze corer (V2A stainless steel, λ_{V2A} = 21 W m^{-1} K^{-1}).

Field investigations

Sediment cores were obtained at Urft Reservoir (50°36′8″N, 6°25′8″O; Germany) in late August 2017 and at Olsberg Reservoir (51°20′54″N, 8°29′17″O; Germany) in September 2017 (Fig. 3). All coring work was conducted aboard a floating platform, which was anchored at the coring position, using a three-point anchoring system.

At Urft Reservoir, four sampling locations along the thalweg from deep water to shallow depths were chosen, to cover a gradient of hydrostatic pressure, GSD, and OM (*see* Supporting Information Table S1 for details). A pair of gravity cores (considered as duplicates) were taken some meters distant from the freeze cores (sampling location 1–3). After retrieving the gravity cores on deck, one core was immediately frozen with dry ice pellets and ethanol, and the other core was capped with a rubber bung and transferred to dark storage. This allows the identification of the freezing process related disturbances on the gas bubble structure with the same sampling technique. At sampling location 4, no gravity core could be obtained due to the high water-saturation of the sediment, resulting in liquefaction of the sample.

Five freeze and five gravity cores were sampled at Olsberg Reservoir. Sampling locations have been selected on the results of previous grab samples, which have shown a different spatial distribution of GSD, OM, and ρ within the reservoir.

Assessment

Core preparation and conditioning

All sediment cores were X-ray CT scanned after sampling in a local hospital. Additional X-ray spectral CT scans of the freeze cores were conducted 5 months after sampling due to the limited temporal availability of this scanner (there exists only one X-ray spectral CT scanner in Germany). Due to this large time difference between sampling and scan, the gravity cores could not be scanned, as an increase in bacterial production probably produce additional gas bubble and therefore causes a bias of the gas content. The core processing is shown in Fig. 4.

X-ray CT data acquisition

The radiodensity for each voxel is commonly reported using the Hounsfield scale (Rogasik et al. 2003). The Hounsfield unit (HU) is calibrated using the absorption coefficient of distilled water (0 HU) and air (−1000 HU). A single energy CT scanner can only reveal the distribution of the linear attenuation coefficient (density), while the spectral CT scanner can represent the distribution of density along with the effective atomic number (Z_{eff}) of each voxel (Iovea et al. 2005). The spectral X-ray CT scanner (Fig. 4) in this study uses one X-ray source and two stacked detectors, rotating around the scanned object which moves longitudinally and provides a sequence of consecutive scan slices, imaging the entire soil sample volume (Ketcham and Carlson 2001). The two radiation detectors allow the detection of X-ray photons with a low and high level of energy. The differentiation enables the detection of Z_{eff}. This allows a determination between water, organic, and inorganic material. Z_{eff} is the average atomic number of the elements inside the voxel like the HU values.

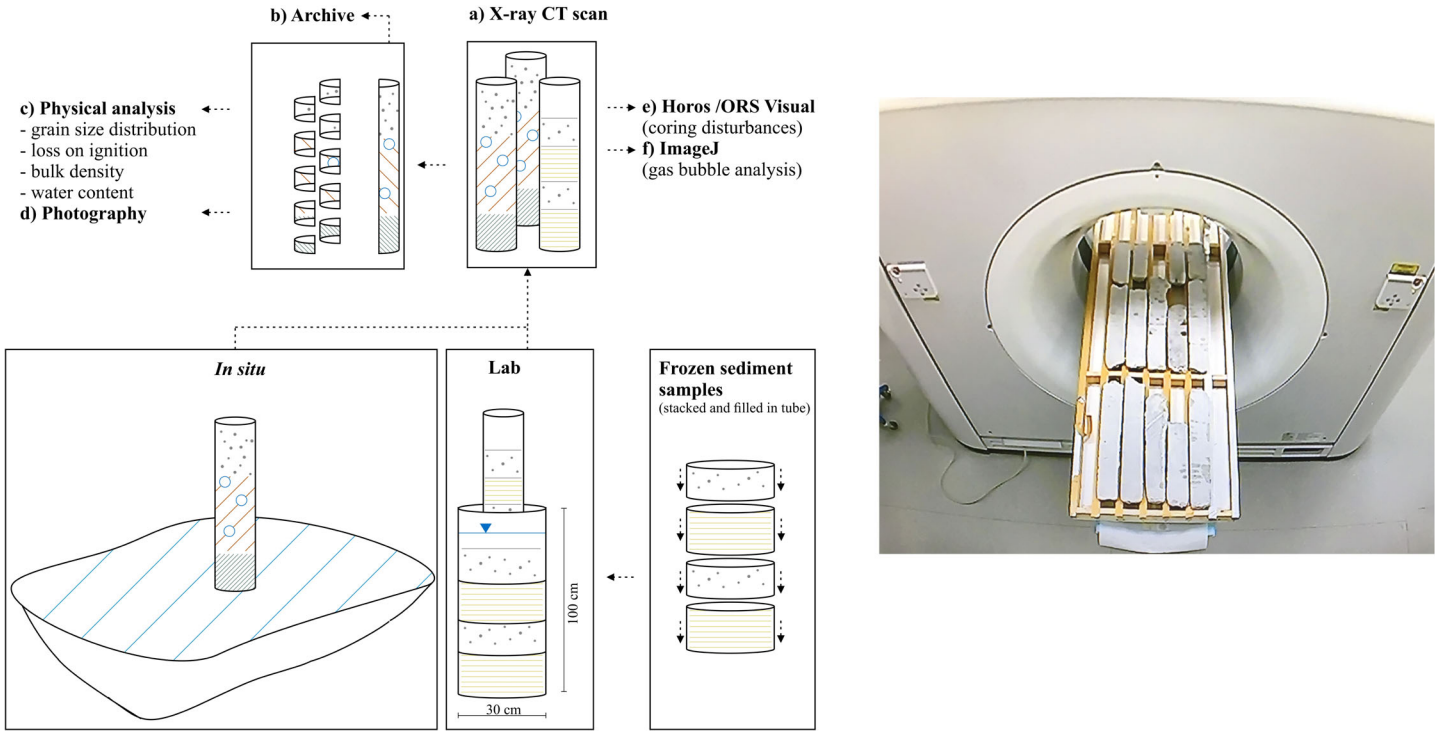

Fig. 4. Right: Philips IQon-spectral X-ray CT (at University Hospital Cologne, Germany) scanner with scanned freeze cores. Left: Schematic representation of the experimental procedure of the field and laboratory investigations: Cores were X-ray CT scanned (a) with a common CT scanner (Siemens AS, 120 kV) and with an X-ray spectral CT scanner (Philips IQon-Spectral CT, 120 kV). The CT scans were analyzed with Horos, ORS visual (e) and gas bubble were visualized with ImageJ (f). After scanning, the cores were split lengthwise with a circular saw into an archive (b) and a working half. The archive half was prepared for photography imaging (d) under natural and UV light (for visualization of the fluorescent pigment layer), and then the extent of vertical displacement was measured. The archive halves were inspected visually with a ZeissStemi SV8 microscope and an attached CCD-camera (Pentax K2). The working halves (c) were defrosted and used for the physical analysis of the GSD, WC, OM, and wet bulk density (ρ).

X-ray CT data treatment

Analyses and visualization of the X-ray CT data were conducted with Horos (Horosproject.org) and ORS Visual Lite software (Object Research Systems). For a qualitative description and measurement of the horizontal and vertical extension of the coring disturbances, and to visualize and analyze the bubble distribution in the sediment cores, a threshold technique, based on the HU and Z_{eff} values, was used. The material in the cores was classified into three categories:

1. "gas bubbles"—gathered all HU and Z_{eff} values associated to gas bubbles. Gas bubble HU values range from −1000 to −500, Z_{eff} is < 5.
2. "ice"—represents all kinds of frozen water. To account for the ice thresholds, calibration samples of different types (water was frozen at different freezing rates) and temperatures were used. Ice HU values ranged from −281 to 167. The ice calibration samples revealed a Z_{eff} value of 7.7.
3. "sediment"—represents all kinds of solid material, ranging from highly organic to inorganic material. The sediment HU ranges from 167 to 3071. Z_{eff} scans clearly reveal the presence of different types of sediments. The corresponding numerical values of Z_{eff} lie between 7.7 (water) and 16.8 (pure quartz), confirming the GSD as well as the mineralogical composition of sediments.

Bubble size (D_{eq}: mean equivalent sphere diameter) distribution and volumetric gas content (θ) in the sediment cores of Olsberg and Urft Reservoir were analyzed using ImageJ. Gas bubbles were segmented in accordance with the intensity distribution of binary images by calculating the fraction of black area on each slice. A constant HU threshold for gas bubbles (−1000 to −500) was chosen for all cores. MorphoLibJ (ImageJ plugin) was used for morphological separation for the CT images of the binary images. Measurement of the 3D gas bubbles is facilitated by counting the number of voxels that constitute it, weighted by the volume of each individual voxel. 3D visualization of gas bubbles was created using the ImageJ 3D volume viewer.

Evaluation of coring disturbances

The vertical cross-sectional X-ray CT images were used to measure the sediment displacement from the initial to the post coring location. The distance between the initial sediment layer and the maximum vertical position after the coring is the *Height of Disturbance* (*HoD*) (Supporting Information Fig. S49).

Based on the assumption that the sediment is generally horizontally layered, the difference in length of the interfacial layer in the disturbed core to the initial horizontal length of the undisturbed core was defined as the *Width of Disturbance* (*WoD*). The percentage of the number of layers affected by coring disturbance is the *Disturbance Occurrence Frequency* (*DOF*). In field cores, especially in gravity cores, the DOF could not be determined for all cores, because the lack of stratigraphic features.

Results and discussion

Freezing rate

The freezing rate experiments revealed clear differences between the temperature dynamics during freezing of the samples, particularly for different WC (Fig. 5). This temporal difference might be due to the thermal conduction differences among the corer (λ_{V2A} = 21 W m^{-1} K^{-1}) and the non-frozen sediment (λ_{water} = 0.6 W m^{-1} K^{-1}) at the transition from the corer to the sediment. The pore water does not start to crystallize until the temperature drops to the temperature of spontaneous nucleation, which is usually a few degrees below the melting point of ice. Initially, the water is in a metastable equilibrium state. At this state, the free water (water that moves under gravity) between the particles freezes and bounds particles. This causes a release of latent heat during ice formation, resulting in a rise in temperature. After the majority of free water is frozen, bound water (unfrozen water film on the sediment particles) freezes and the sediment particles start to cool down. The increase of the thermal conductivity after the phase transition from water to ice (λ_{ice} = 2.3 W m^{-1} K^{-1}) results in an acceleration of the freezing process. This effect can be observed at the phase transition, where the negative gradient of the curve increases for all samples (Fig. 5). The slope of the curves is related to the (bound) WC. The smaller the particles, the higher is the specific surface area and therefore a higher amount of unfrozen water can exist at temperature below the freezing point, which increases the time until the sample is completely frozen. This effect can be shown exemplarily in the temperature profile of *Olsberg Sediment* and *Urft Sediment* (WC: 72% and 69%), which have a significant higher WC than *Silt/Sand Sediment* (WC: 27% and 28%). Other parameters (e.g., salinity, mineralogy) may also influence the freezing time. However, the number of variations within the sediment parameters in this study is too small to draw a clear conclusion of the relevant parameter and to separate the effects of individual parameters and should be investigated in future studies.

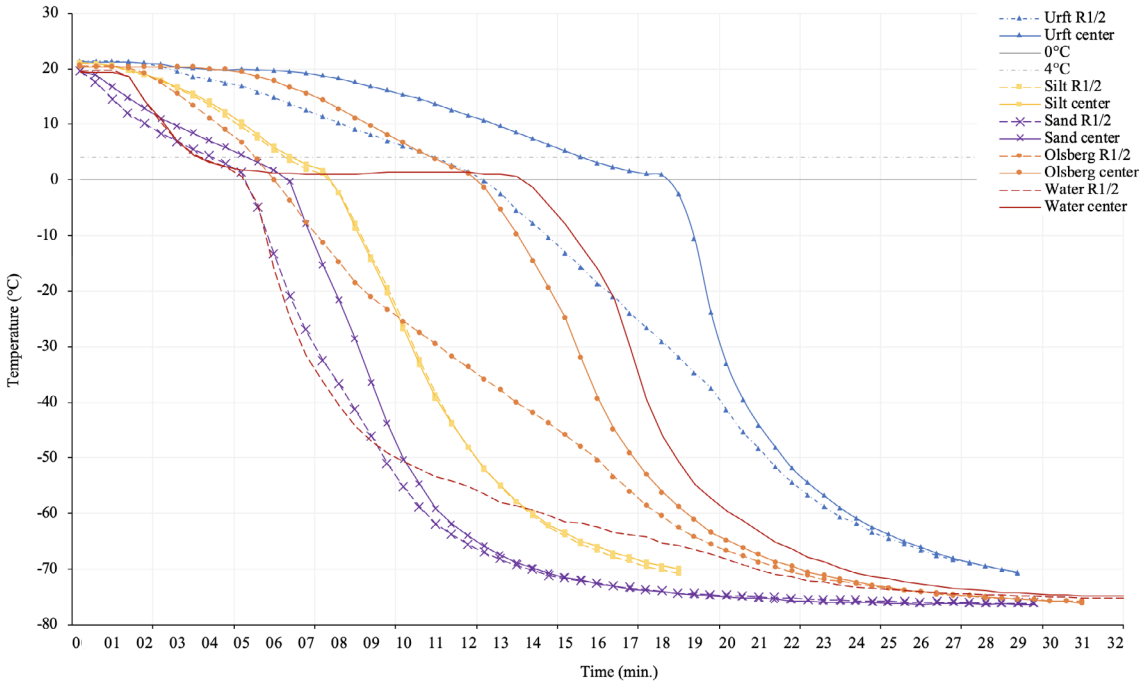

Fig. 5. Time series of sediment temperature during freezing of *Silt Sediment*, *Sand Sediment*, *Olsberg Sediment*, and *Urft Sediments*, as well as tap water as a reference. The temperature was measured in the center of the core (solid lines) and at a radial distance of 18 mm from the core center (*R*1/2, dotted lines). The time needed to cool down the sample from 0°C to −70°C varied from 07:36 min for *Sand Sediment* to 16:00 min for *Urft Sediment*. The freezing rates of all samples varied from −14.8°C min^{-1} (*R*1/2) to −22.6°C min^{-1} (center). *Urft Sediment* has shown the slowest freezing rate (−0.6°C min^{-1}) during liquid state, and also the fastest freezing rate (22.6°C min^{-1}) in the center after phase transition from water to ice. After phase transition, the freezing rate of all samples increased. The higher the WC, the slower the freezing rate. A surprising result was that the time difference between the *R*1/2 and center of pure water was highest of all samples.

The freezing rate results provide information about the time, which is required to entirely freeze the sediment samples under in situ conditions, to reduce the risk of a loss of the sample and to prevent the sediment structure being affected by changes in hydrostatic pressure and temperature. Furthermore, the freezing rate results allow to determine the probability of particle and bubble migration, as well as gas bubbles nucleation at the water-ice interface, when the concentration of dissolved gas reaches a critical value. Hung et al. (1997) and Lee and Hsu (1994) found that the freezing rate has a significant impact on particle migration in terms of dewatering of sludge by freeze-thaw treatment. However, particle migration is a complex phenomenon affected by many important variables besides the freezing rate, such as particle size, shape, and dissolved solids concentration (Halde 1980). Due to mutual interactions between these parameters, a "critical velocity", where particles are rejected or entrapped at the propagating freezing front cannot be determined. It can be concluded that the higher the freezing rate is, the lower is the risk of dislocation of sediment particle. A high freezing rate also reduces the size of gas bubbles that may form by nucleation at the water-ice interface (Carte 1961) if the ice-water interface becomes supersaturated (Boereboom et al. 2012). According to Lipp et al. (1987), the maximum radius of nucleated bubbles is $< 20\ \mu$m at a freezing rate $> 90\ \mu$m s^{-1}, and therefore smaller than the spatial resolution of the used X-ray CT scanner. Generally, the higher the freezing rate, the less time is available for bubble growth after nucleation, that is, before the bubbles

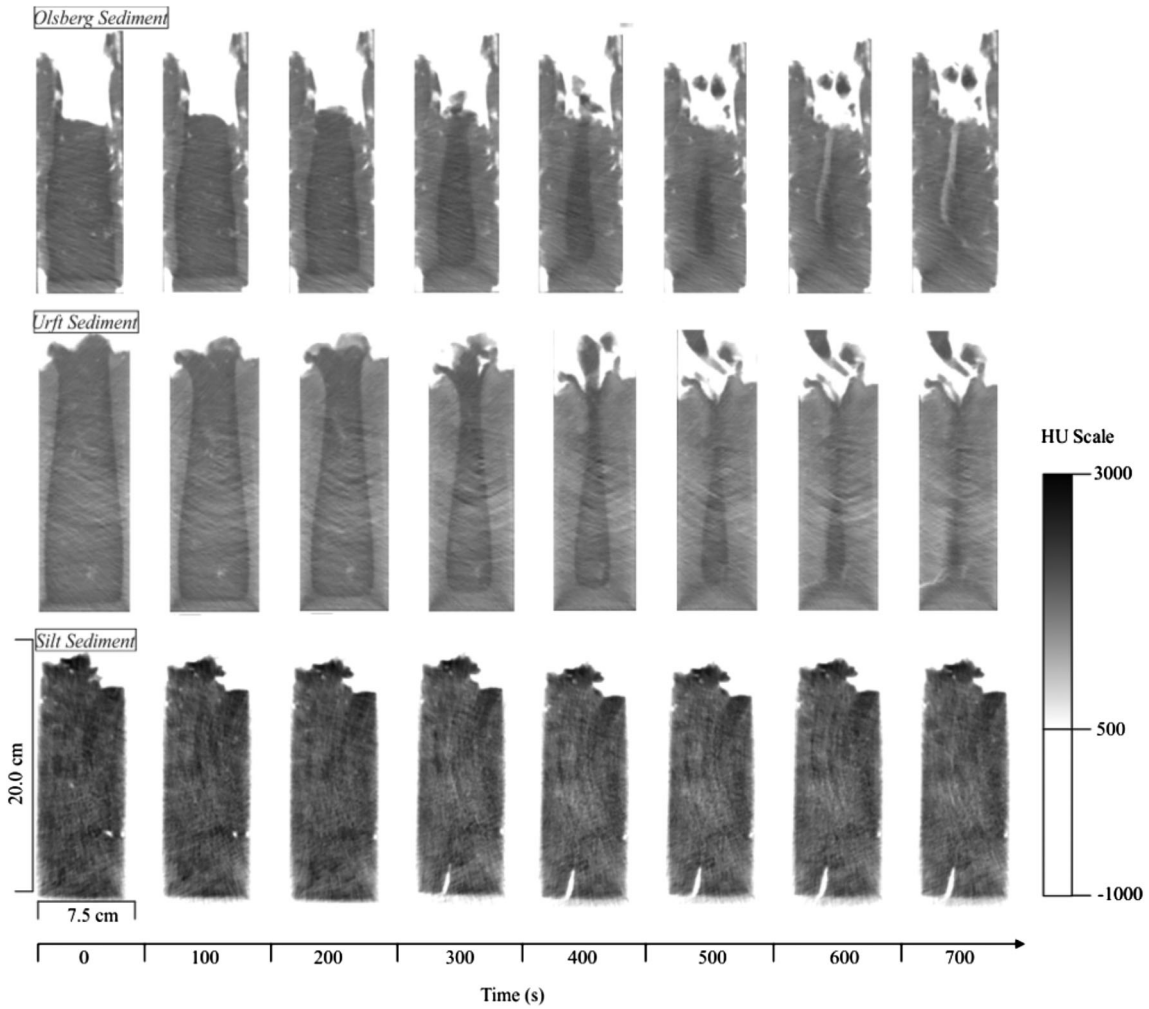

Fig. 6. Image sequence of the real-time CT scans of *Olsberg Sediment*, *Urft Sediment*, and *Silt Sediment* shown as vertical cross-sectional CT scan images. *Olsberg Sediment* and *Urft Sediment*: The continuous volume expansion due to the change in sample temperature and the rapid expansion at phase transition resulted in a vertical displacement of the sample in the center of the core. The displacement takes place in the direction of least resistance, as the sediment column freezes from the out- to the inside. Temperature of the dry ice and ethanol mixture is lowest at the surface of the coolant between the double-walled tube, where the sublimation of dry ice takes place. This results in a conical freezing front (sharp interface in gray scale), which gradually converges from the top to the bottom of the sample. *Silt Sediment*: The sediment was completely frozen in a shorter time (t = 200 s) than *Olsberg Sediment* and *Urft Sediment* (t = 700 s). No conical shape can be seen in the images. The expansion of water caused a burst of the graphite pipe, which is shown as a crack at the lower left side of the pipe at t = 300 s.

become encapsulated in ice. Existing knowledge on bubble nucleation during freezing, however, is based on measurements in pure water. The effect of the sediment matrix on the nucleation microbubbles has not been investigated. This is an issue for future research to explore.

Real-time CT scans

The observations of the real-time CT scans (Fig. 6) revealed that a higher WC correlates to a slower freezing process and corroborates to the findings of the freezing rate experiments. The results have shown that *Silt Sediment* was frozen almost instantly throughout the entire horizontal cross-section, whereas a slowly propagating freezing front from the outside to the inside of the core was observed in the *Olsberg* and *Urft Sediment* cores. This slow freezing process results in a slightly change in density. This change in density is shown in the vertical cross-sectional CT scan images (Fig. 6) in a darker shade of gray in the center of the core (HU = 270), indicating a higher density after the freezing process in this region in contrast to the HU value of the entire core before freezing (HU = 245). The lateral shift in density may result from the crystallization process of the pore water. Growing ice crystals can displace solid particles and cause a rearrangement of the soil matrix (Singh and Niven 2013), which depends mainly on the freezing rate. There are three modes how sediment particles are affected by the freezing front: The freezing front pushes the sediment particles and segregates them in the last-freezing liquid or engulf particles after having pushed them over some distance or may engulf the particles instantaneously upon contact (Lipp et al. 1987). Vesilind and Martel (1990) stated that various research studies confirmed that the smaller the solid particles, the more likely they are moved by advancing ice front, and, that the risk of particle relocation increases with decreasing freezing rate. Our findings are in accordance with those previous studies and show that an increasing WC negatively affects the uniform distribution of the density within the sediment column. Additionally, increasing WC and the related, relatively slower freezing rate increases the vertical displacement of sediment layer in an upward direction.

Coring disturbances

Bending

The results showed that both the freeze and gravity core samples are affected by bending, which can be identified as layer deformation at the outer perimeter of the corer (Fig. 7a–c). The DOF of the freeze cores is 31 ± 19 (mean and standard deviation) for *Silt Sediment* ($n = 9$) and 41 ± 12 for *Silt/Sand Sediment* ($n = 6$), whereas the DOF of the gravity cores is 14 ± 12 for *Silt Sediment* ($n = 3$) and 62 ± 2 for *Silt/Sand Sediment* ($n = 2$). *Olsberg Sediment* showed no significant bending for both corer types. WoD of the freeze cores is 5 ± 3 mm for *Silt Sediment* and 5 ± 1 mm for *Silt/Sand Sediment*, and therefore slightly higher than of the gravity cores with 3 ± 3 mm and 5 ± 0 mm, respectively. The HoD of the freeze cores is 3 ± 2 mm for *Silt Sediment* and 4 ± 1 mm for *Silt/Sand Sediment*, and slightly smaller than of the gravity cores with 4 ± 4 mm and 4 ± 1 mm, respectively. WoD and HoD vary considerably within a single core, where bending occurs more frequently in the upper half of the core than in the lower half. We speculate that this might be due to an increase in the frictional drag between the sediment and core liner with increasing penetration depth, as described by Skinner and McCave (2003). A constant penetration velocity increased the intensity of bending compared to an inconstant penetration velocity (Supporting Information Figs. S9–S37).

Field freeze cores showed no bending (Supporting Information Figs. S38–S46), whereas Urft and Olsberg Reservoir gravity cores showed a DOF of 100%, with WoD of 11 ± 4 mm and HoD of 7 ± 4 mm, where bending occurs predominantly in the lower half. This might be related to the reduced penetration force of the freeze corer due to the sharper design of the cutting-edge in contrast to the gravity corer. This assumption is in line with previous findings of Hvorslev (1949) showed the importance of the details of the cutting-edge design. This is in line with Clayton and Siddique (1999) who found that the most important factor governing coring disturbance is the combination of area ratio (ratio of displaced sediment area to the total sampler area) and cutting-edge angle (Clayton and Siddique 1999). A reason for this rather contradictory result that bending occurs predominantly in the lower half of the cores compared to the laboratory results is not entirely clear. We assume that the consolidation of the in situ sediment increases with depth and therefore the frictional drag between the sediment and core liner increases, respectively. Consolidation in the laboratory cores was not given.

Smearing

DOF for freeze cores without ice crust (0–13%) was significantly smaller than cores with ice crust (30–50%; Fig. 7d,e,h) and that of the gravity cores in *Olsberg Sediment* (31.3%). This might be related to the higher roughness of the ice crust surface in comparison to the stainless steel of the freeze corer and the PVC material of the gravity corer. The higher roughness causes a higher friction, which leads to enhanced shearing of sediment in direction of penetration. The maximum WoD of 13 mm and the maximum HoD of 39 mm of the freeze cores can be found in relatively short distances toward the core liner (e.g., Supporting Information Figs. S26, S30). Smearing can clearly be distinguished from bending, as the HoD is significantly higher and the WoD is smaller. This relies on the fact that smearing is an effect of dragging material along the core tube wall between adjacent sections into deeper layer (Chant and Cornett 1991).

Smearing in the field cores has only been observed in *Urft_FC2_Tripod_7* (Fig. 8), which has the thickest ice crust of all in situ freeze cores. This ice crust formed during the descent of the corer, which took about 1 min. The results from the field investigation are consistent with those from the laboratory, where smearing predominantly appeared when an ice

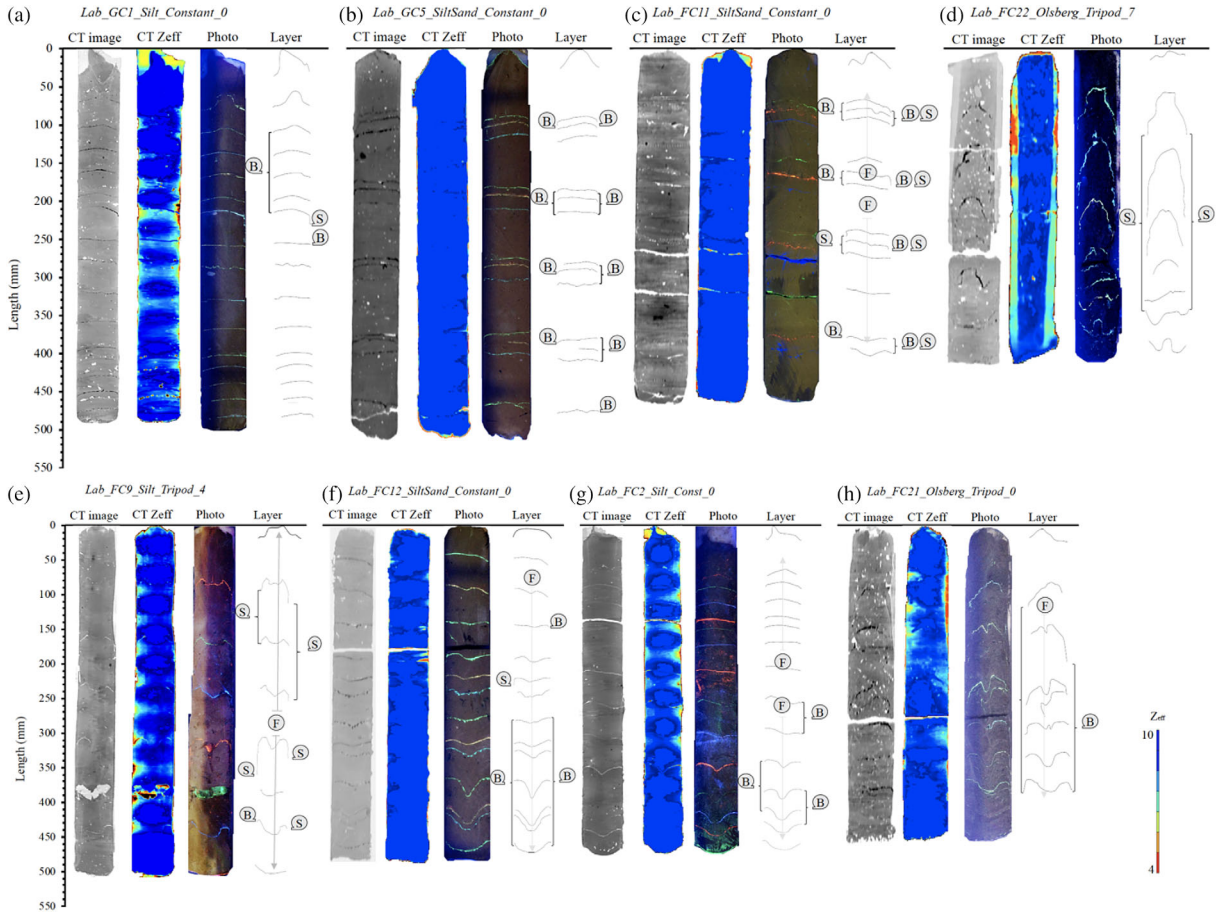

Fig. 7. Selected laboratory cores (from left to right: X-ray CT scan image, Z_{eff} CT scan image, core photography under UV illumination, and digitized sediment layer) with artificially fluorescent laminated stratigraphy, shown as colored lines in the photos. To better visualize the coring disturbances, the layers have been digitized and labeled with the corresponding type of disturbance for each core. Four major types of disturbances were observed: (1) bending (B); (2) smearing (S); (3) freezing (F) (shown as an arrow in upward- and downward-direction) and (4) shortening. (**a**–**c**): Bending: Sediment layer are concavely formed and slightly bended downward at the core margin; (**d**) Smearing: Strong deformation due to shearing of the ice crust (which can be differentiated in the Z_{eff} CT scan images; Z_{eff} ranges from 7.2 to 7.4 for ice) against the sediment which occur in close distance to the rim of the core; smearing drags the sediment significantly downward along the core margin; (**e**) Smearing: Moderate deformation due to shearing of the freeze corer without ice crust against the; (**f**) Freezing: Vertical displacement of the sediment layer in downward direction. HoD increases with depth; (**g**) Freezing: Upward vertical displacement at the upper half and downward displacement at the lower half of the core. HoD increases with increasing depth (**h**) Freezing and Smearing: Upward displacement at the upper half and downward displacement of the layer in the lower half of the core. Smearing is the result of the friction between the ice crust and the freeze corer. The complete documentation of all laboratory experiments, including WC, penetration velocity, as well as incremental and cumulative shortening diagram are shown in the Supporting Information Figs. S9–S37.

crust on the inside of the corer increased the shearing force between the sediment.

Freezing

All laboratory freeze cores (Supporting Information Figs. S9–S30) showed a vertical displacement of the sediment layer, which is probably the result of the freezing process, caused by radial freezing process from the outside to the inside of the core. It can be ruled out that the vertical deformation of the sediment layer in freeze cores is the result of friction between the corer and the sediment and can be clearly differentiated from bending and smearing (Fig. 7f–h). Such deformation would appear as downward bends at the outer perimeter of the sediment core, which increases radially from the center of the core (Acton et al. 2002). An inconstant penetration velocity increased the DOF. *Olsberg Sediment*, which has a significantly higher WC shows the highest DOF of 61–78%, whereas DOF of *Silt Sediment* and *Silt/Sand Sediment* of 46–63% is slightly lower. HoD of all laboratory freeze cores is 34 ± 6 mm and WoD is 12 ± 4 mm.

This finding corroborates to the observation of the real-time CT scans, which have shown that the vertical displacement is a result of the expanding ice volume, primarily at phase transition from water to ice, which "squeezes" the nonfrozen inner part of the core in the direction of least resistance. Our observations are in line with the concept of the freezing-induced deformation in soils, described by Grechishchev (1972, 1973). He distinguished three different

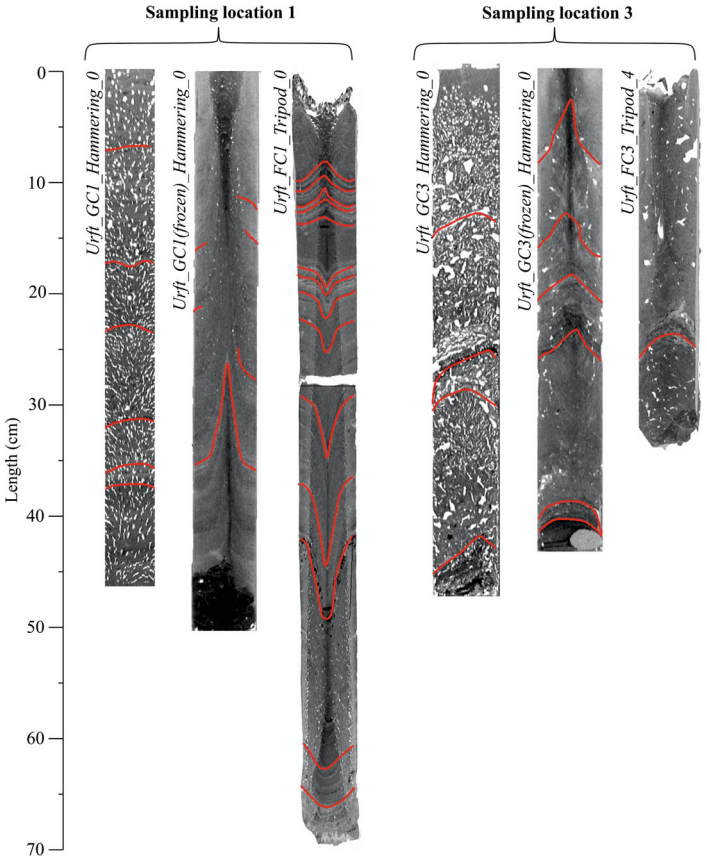

Fig. 8. Vertical cross-sectional X-ray CT scan images of Urft Reservoir sampling location 1 and 3. Gray scale bar shows HU scale. Gas bubbles are shown as white spots. Core top is at 0 cm and indicates the position of the sediment–water interface. Coring disturbances (marked as red lines) are seen on all cores. Urft Reservoir gravity cores (*Urft_GC1_Hammering_0* and *Urft_GC3_Hammering_0*) shows bending at the core margin. Of particular note is the orientation of the bubbles in both gravity cores towards the core edge, originating from the symmetry axis of the core. This might be a result of a partial mid-core flow-out during withdrawal of the core. The adherence of the sediment at the core liner is higher than in the center of the core and therefore, the inner part of the core is more likely to flow out to a larger extent that the outer part. Freeze cores and frozen gravity cores show an upward displacement due to freezing process, except *Urft_FC1_Tripod_0* where the displacement is also in downward direction.

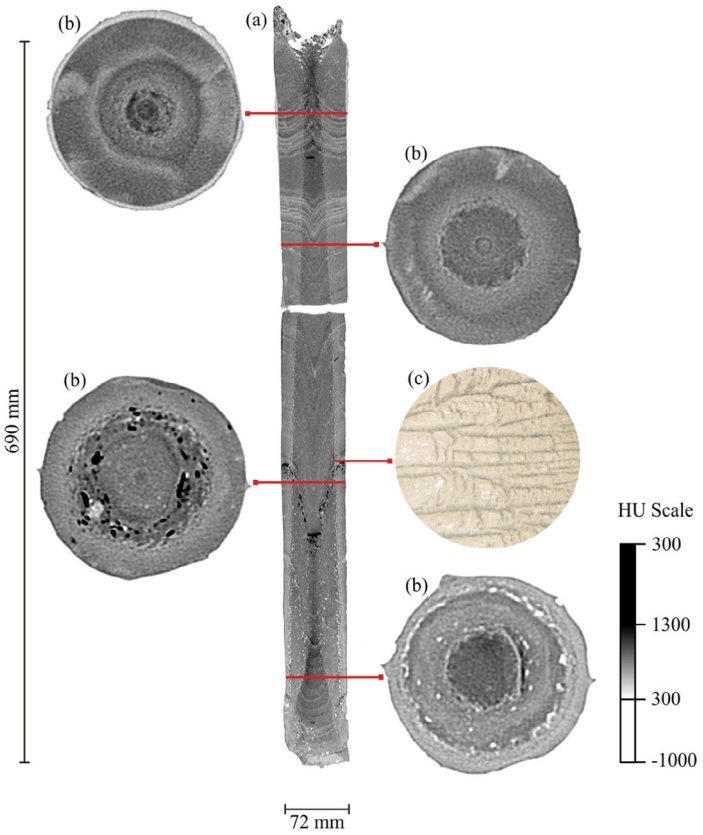

Fig. 9. Vertical (a) and horizontal (b) cross-sectional CT scan images (HU scale according to the color bar) at different depths and microscopic pictures (c) of ice spikes formed in core *Urft_FC1_Tripod_0*. Core top is at 0 cm and indicates the position of the sediment–water interface. The cross-sectional images show a circular arrangement of solid particles (black spots) and gas bubbles (white spots), which may have formed during the freezing process. Of particular importance is the up- and downward vertical distortion of this core structure. The layers in the upper 13 cm are bent in an upward direction with a maximum WoD of 17 mm and a maximum HoD of 41 mm, whereas the layers below 13 cm depth are bent in a downward direction with a maximum WoD of 42 mm and a maximum HoD of 75 mm. The HoD upward and downward distortions increase with increasing core depth. The point, where the vertical displacement occurs, coincides with a sharp gradient of different X-ray absorption. This can be seen as a conical shape within the vertical cross-sectional image. HU values with a darker shade of gray are located inside of the conical arrangement (HU = 400 $\pm$ 150), whereas a brighter shade of gray (HU = 286 $\pm$ 127) can be seen outside.

multidirectional processes: Linear expansion (or contraction) of the soil-forming components, the continuous phase transition at the ice-water phase boundary, and the thermal deformation of the internal microstructures. Because expansion within the steel framed freeze corer is limited to the vertical direction, and the cores are frozen from the outside to the inside, the inner part of the core can only be relocated up- or downward. This phenomenon has been described by Rutledge and Fleeger (1988), who found that the extent and shape of distortion strongly depend on the freezing rate. Accordingly, the fast freezing rate results in a significantly higher DOF, WoD, and HoD (e.g., *Olsberg Sediment*).

Figure 9a shows a conically shaped area in the vertical cross-sectional CT scan image of *Urft_FC1_Tripod_0*. Horizontal cross-sectional CT images (Fig. 9b) show that this area is bounded by accumulations of solid particles and gas bubbles. This observation corroborates the hypothesis of Stephenson et al. (1996), who stated that ice crystal formation causes a flux of sediment pore water, excluding some solids. The boundary, where the circular arrangement occurred, also shows ice spikes (Fig. 9c), which can be seen in the microscopic images. Ice spikes grow as tiny cracks in a radial direction from the core margin towards the center of the core, where spikes increase in size (maximum length of 6 mm) and decrease in number. Parker et al. (1996) stated that ice spikes can grow into the still unfrozen sludge in

the direction of freezing at high freezing rates (> 21 μm s^{-1}), generally bypassing the sludge flocs, apparently without moving or altering them (Parker et al. 1996). The occurrence of ice spikes (Fig. 9) is consistent with our observations of the freezing rate experiments, which showed a freezing rate of > 20.8 μm s^{-1}. We have verified that by using microscopy images and produced similar results (e.g., Supporting Information Figs. S10, S11, S16, S24) where the conical shape coincided with the interface in the HU values. The results (Fig. 9) also indicate a lateral displacement of gas bubbles from the outer perimeter into the center of the core, where gas bubbles are circularly arranged. It cannot be ruled out that those gas bubbles originated from gas bubble formation from dissolved gas due to the phase transition. In this study, it cannot be excluded that nucleated gas bubbles grew or merged to form larger bubbles. According to Lipp et al. (1987), the maximum radius of nucleated bubbles is < 20 μm at a freezing rate > 90 μm s^{-1}. This bubble radius is significantly smaller than the spatial resolution of the X-ray CT scans (voxel size: 0.1263 mm^3).

Beside core *Urft_FC1_Tripod_0*, the shape of the layer distortion to other Urft Reservoir cores significantly differs by showing a more uniform expansion over the whole length of the core, with a WoD in an upward direction of 51 mm and a HoD of 23 mm. The effect of uniform expansion was also observed at Olsberg Reservoir freeze cores and in the real-time CT scans with *Olsberg Sediment*. The cores have WoD of 36 ± 6 mm and a HoD of 16 ± 6 mm. However, no correlation has been observed between the direction and extent of the layer displacement and WC, OM, and ρ (Supporting Information Figs. S38–S46). This might be due to various sediment properties, which may influence each other and either enhance or mitigate the effect of freezing on the sediment structure.

Shortening

DOF of the freeze cores was 17% ± 20%, whereas the gravity cores showed a higher DOF, but with a lower variation with 30% ± 14% (Table 1). The DOF of the freeze core shortening for *Olsberg Sediment* (48%) was significantly higher than for *Silt Sediment* (28%) and *Silt/Sand Sediment* (25%). This finding of the current study do not support the results of Blomqvist (1991), where clayey and silty sediments are shortened more than light, unconsolidated sediments, such as *Olsberg Sediment*. DOF of gravity core shortening for *Silt/Sand Sediment* (22%) and *Olsberg Sediment* (37%) was lower than the freeze cores, whereas *Silt Sediment* is only marginally higher (30%). The gravity core shortening results are consistent with those of Morton and White (1997), who found a shortening factor of 30%, and inconsistent to earlier findings of Emery and Dietz (1941), and Emery and Hülsemann (1964), who reported a shortening factor of up to 50%. However, our findings show that shortening increases with WC and OM, and support the idea of Emery and Dietz (1941) that the degree of shortening depends on sediment characteristics.

Our results showed that the shortening pattern (see bar charts, showing the shortening pattern in Supporting Information Figs. S9–S37) in the laboratory experiments is not uniform throughout the core. The best correlation between shortening and physical sediment properties was found where GSD and WC changed within two subsequent sediment layers, which is given for *Silt/Sand Sediment*. Half of the cores exhibited this pattern, which is shown as a stair-step pattern of alternating vertical lines and horizontal lines, representing the unshortened and shortened sections (Morton and White 1997). Besides this finding, we observed different shortening pattern, however, show poor correlation with WC, OM, and GSD is given (Supporting Information Figs. S38–S46).

Measurement of the in situ gravity core shortening was not possible, as stated by Kallstenius (1958) and Blomqvist (1991). No information of the effect of tilting and disturbances related to the penetration process and withdrawal could be obtained, as no observation during those processes was possible. Though, the freeze corer in combination with the tripod allowed the measurement of the in situ core shortening. However, even though the careful descend of the freeze corer was controlled by video monitoring, a hydraulic shock wave in front of the cutting-edge washed away a certain part of the flocculent surficial sediment layer at one sampling location (Supporting Information Fig. S8). As the descending velocity of the gravity corer is much higher than the one of the freeze corer, it can be assumed that core shortening and a hydraulic shock wave of the gravity corer occurs more frequently and washes away more flocculent surficial material, resulting in coring disturbances.

Gas bubble analysis

3D gas bubbles visualization of Urft and Olsberg Reservoir freeze and gravity cores shows that the volumetric gas content (θ), bubble size, and bubble distribution vary significantly between the sampling locations and different types of coring techniques (Fig. 10). It is obvious that gas bubble distribution and size did not follow a general pattern. For instance, bubbles in *Urft_FC1_Tripod_0* were found 5 cm below the sediment–water interface and below a depth of 40 cm, whereas the gravity core gas bubble distribution is almost constant over depth.

θ of Olsberg Reservoir gravity cores (4.5–12.4%) was significantly larger than of freeze cores (0.6–1.2%) at sampling depths between 0.8 and 2.5 m (Fig. 10). θ of Urft Reservoir gravity cores decreases with decreasing water depth of the sampling locations, from 10.5% (31 m), 11.2% (22 m), and 10.9% (10 m), respectively. In contrast, θ of Urft Reservoir freeze cores increased from 0.2% (31 m), 0.2% (22 m), 2.0% (10 m) to 1.2% (5 m) with decreasing water level. θ of the frozen gravity core shows a similar trend, 0.3%, 2.9% to 5.6%, respectively. The increasing θ from deeper to shallower parts of the Urft Reservoir corresponds to the findings of Bastviken et al. (2008), Duc et al. (2010), Natchimuthu et al. (2016), Wik et al. (2013), where ebullition is often found most active in

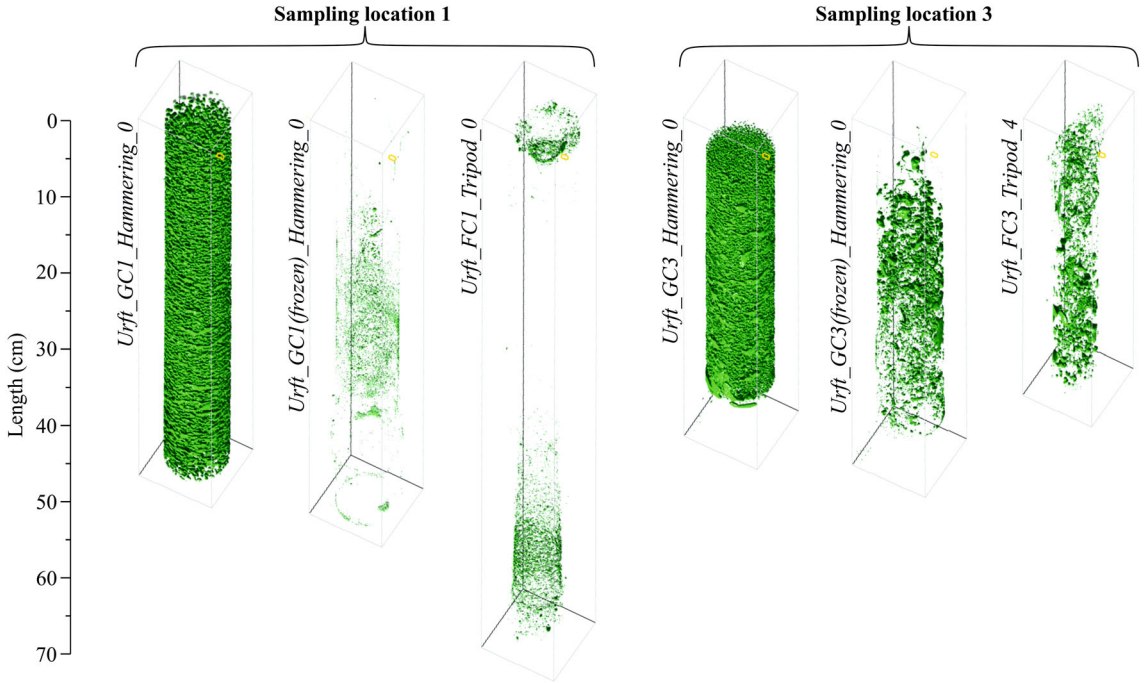

Fig. 10. Exemplary 3D gas bubble visualization in gravity, frozen gravity, and freeze cores of Urft Reservoir sampling locations 1 and 3 (see labels). In the gravity cores, gas bubbles are homogenously distributed over depth, whereas the gas distribution in the freeze and frozen gravity cores are different and more heterogeneous and obviously do not correlate to the gravity cores. Differences are more pronounced at sampling location 1 in contrast to sampling location 3, due to the greater differences in hydrostatic pressure and sediment temperature.

the littoral zone. The greater variability in θ between the three different coring techniques of Urft Reservoir in comparison to Olsberg Reservoir may be related to the deeper water depths and differences between the lake-bed temperature ($T_{\text{Urft,Dam}}$ = 5.1°C, $T_{\text{Urft,Inflow=}}$ 7.9°C, T_{Olsberg} = 14.2°C) and ambient air temperature (T_{Olsberg} = 24.3°C; T_{Urft} = 21.2°C) of the thermally stratified Urft Reservoir. This may be explained by the observations of Lane and Taffs (2002) and Scandella et al. (2011), who found that the core can expand, and sediment structures disturbed by the expansion of gas bubbles due to the decrease in hydrostatic pressure during core recovery. Also, the decrease in hydrostatic pressure causes a considerable shift in the partitioning between dissolved CH_4 and the gaseous phase. CH_4 dissolute, as saturation concentration decreases significantly with pressure (Duan et al. 1992) and temperature. Additionally, even though the gravity cores were transported in a dark transport box, the temperature is higher than the in situ temperature of the sediment, and movements and vibrations during transport cannot be excluded, which may cause ebullition and bias the gas bubble characteristics. It might be also be attributed to an additional methane formation, as the methanogenesis is temperature-dependent (Yvon-Durocher et al. 2014). Wilkinson et al. (2019) demonstrate that a 10°C temperature change can cause between a 1.6-fold and sevenfold change in methane production rate. Due to the short time difference (approximately 36 h) between sampling and CT scan, the effect of increasing methane production can be assumed to affect θ, but to a minor extent. When comparing our results to those of Dück et al. (2019), who showed that freezing of gassy clay sediments under laboratory conditions caused a contraction in θ by 27% ± 6%, it can be concluded that the greater differences in our study can be related to the changes in hydrostatic pressure and sample temperature, as described above.

Bubble size (D_{eq}) was significantly smaller in the freeze cores (0.2–1.0 mm) and frozen gravity cores (0.1–1.0 mm) than in gravity cores (1.0–2.1 mm) at Urft Reservoir (Fig. 11). For instance, *Urft_GC3(frozen)_Hammering_0* contained few large bubbles, resulting in a relatively smaller θ, comparing to *Urft_GC3_Hammering_0*. D_{eq} of the freeze core increased from 0.2 (31 m depth), 0.3 (22 m depth), 0.9 (10 m depth) to 1.0 mm (5 m depth), and in the frozen gravity cores from 0.1, 0.4 to 1.0 mm with decreasing water depth. This trend in bubble size was not observed in the gravity cores (ranging from 1.0, 2.1 to 1.1 mm from deep to shallow water depths). The same discrepancies in gas bubble distribution between frozen and unfrozen sediment cores were observed at Olsberg Reservoir. D_{eq} of Olsberg Reservoir freeze cores (0.2–0.6 mm) was significantly smaller contrast to gravity cores (0.9–2.0 mm) at water depths between 0.8 and 2.5 m.

Freezing can be expected to result in gas bubbles nucleation due to the two orders of magnitude smaller gas solubility in

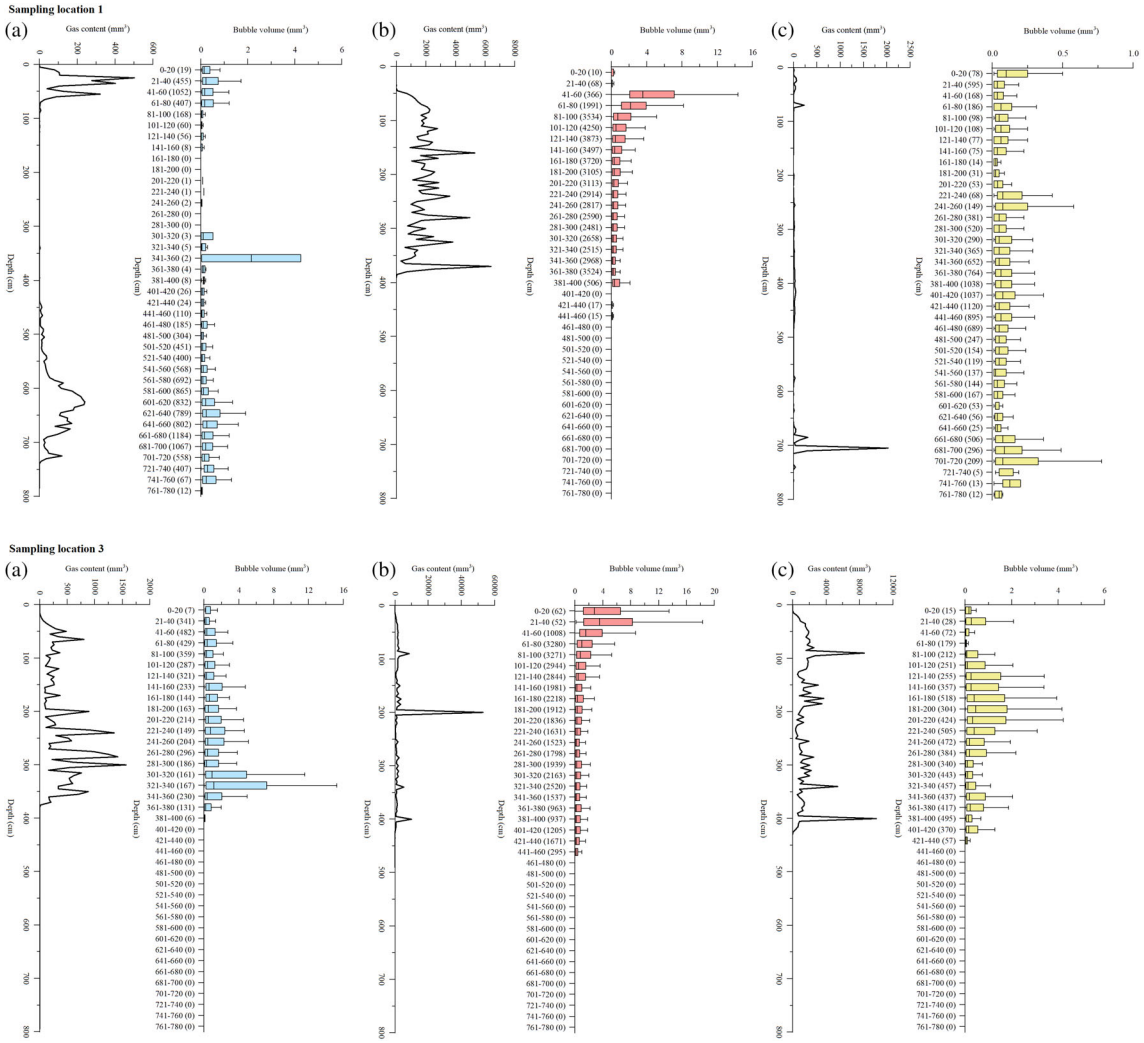

Fig. 11. Gas bubble size and volumetric gas content (θ) as a function of depth for Urft Reservoir sampling location 1 and 3. (a) The sediment freeze core, (b) the gravity core, and (**c**) the gravity core (frozen) plots, respectively. Bottom and top of boxes show 25th (first quartile) and 75th (third quartile) percentiles, respectively. Whiskers show maximum and minimum.

ice compared to water (Killawee et al. 1998). Due to the limitation in spatial resolution of the CT scan, the occurrence of this effect can neither be confirmed nor denied. In future investigations, real-time CT scans with a higher spatial resolution may shed some light on this issue of nucleation and/or relocation of gas bubbles due to the freezing process.

Conclusions

This study determined the causes, effects, and extent of coring disturbances between freeze and gravity coring techniques in comparative laboratory and field investigations. We demonstrated that the novel freeze coring technique facilitates an effective way for obtaining gas-bearing sediment samples and the combination with the nondestructive X-ray CT scans made a visualization of the in situ sediment structure and gas bubble characteristics possible. Our findings suggest that this freeze corer combined with X-ray CT analysis may open a new field for comparatively cost-efficient studies requiring a qualitative and quantitative understanding of the structure and quantity of gas bubbles in aquatic sediment. Spectral X-ray CT scans can provide additional information for the analysis and interpretation of sediment cores, which increases the informative value of existing X-ray CT scans (e.g., differentiation between organic and inorganic material).

Nevertheless, almost all cores showed coring disturbances and it was also shown that the identification of zones of coring disturbances is necessary, as this facilitates a necessary correction of analysis results. We identified four major types of coring disturbances: bending, smearing, freezing, and shortening. Minor disturbances (e.g., tilting, liquefaction) can be assumed also to occur; however, a clear identification or separation to other disturbances is often difficult due to missing appropriate measurement techniques.

The freeze coring technique reduces the risk of coring disturbances during core recovery, depressurization, and handling. The design of our freeze corer prevents the typical conical shaped form of cores, which usually occurs by using tube- or wedge-shaped freeze corer (DIN ISO 2016). By using the tripod and underwater video camera, it is possible to prevent the corer from being affected by tilting, allows the measuring core shortening and observation of the penetration process, where a possible gas release can be detected. Our results suggest that freezing the sediment in situ preserves the gas characteristics better than the gravity coring technique. Due to the limited data on the gas bubble distribution in both investigated reservoirs, further research is needed to validate the results of the results obtained with the freeze coring technique to characterize gas bubbles in aquatic sediments under different conditions (e.g., water depth, sediment composition) and compare those results with other coring methods (e.g., pressurized corer). Freeze coring affects the sediment stratigraphy in a regular way, that is, by a gradual shifting of the inner relative to the outer part of the core. Such a gradual disturbance does not affect the general integrity of the sediment. Therefore, it is important to consider that gas bubbles and particles are rearranged due to the freezing process, and, freezing may result in the nucleation of gas bubbles that were not resolved in the X-ray CT measurements and should be investigated in future studies.

No type of sediment coring technique is applicable to all types of studies and conditions (Glew et al. 2001). Based on the results and experiences made within this study, we can state the following recommendation for the use of freeze and gravity coring:

1. The probability of a change in volumetric gas content, equivalent sphere bubble diameter, and sediment stratigraphy due to the change in hydrostatic pressure during core recovery and sample temperature increases with sampling depth. To eliminate potential bias, the use of the freeze coring technique in low-cohesive and gas-bearing sediment is recommended. This recommendation is supported by results from field investigation, which showed that the discrepancies in θ and D_{eq} between the gravity and freeze core increase with increasing hydrostatic pressure and difference in sample temperature.
2. Our results suggest that nearly all cores are affected by different types and extents of coring disturbances. The occurrence and extent of coring disturbances are highly variable and differs significantly between the coring techniques and boundary conditions. Undetected coring disturbances would lead to analytical bias resulting in possible erroneous or inaccurate conclusions. Therefore, the validity of various results obtained from field cores is questionable (e.g., Baxter et al. 1981; Blomqvist 1985; Buckley et al. 1994; Ostrovsky 2000). The extent of sampling bias will largely be the result of the choice of corer design, water depth, and physical properties θ and of the sediment. With increasing water saturation, gravity coring has shown to be more susceptible to (partial) leakage or liquefaction during core recovery and for problems during sample handing in the laboratory. Thus, the freeze coring technique should be used for water-saturated sediment to prevent liquefaction. This leads to the conclusions that the analysis of core-specific disturbances is highly recommended and should become a routine aspect of data analysis and publication reporting, dealing with sediment core data. We recommend a core-specific analysis of the type and extent of coring disturbances on the structural integrity of the subsequent analysis, as suggested by Liernur et al. (2017). A visual inspection of the core stratigraphy and an exclusion of a buffer zone around the corer (e.g., Franchini and Zeyer 2012; Strasser et al. 2015) only allow the identification of coring disturbances in texturally and structurally homogenous sediments of just one cross-section through the core, and does not take into account the spatial structure of disturbances.
3. Core shortening is an important disturbance for both the gravity and freeze coring techniques. The laboratory experiments indicate that core length has been changed during the penetration and withdrawal process, where the gravity coring technique seems to be more pronounced to shortening than the freeze coring technique. As the degree of core shortening is related to the core tube diameter, penetration velocity (Emery and Dietz 1941; Hvorslev 1949; Hongve and Erlandsen 1979; Blomqvist 1985, 1991), and sediment parameter, it is important to measure the penetration depth in situ. This allows adjusting the core stratigraphy to remove the effect of shortening to their natural position to reduce the risk of an under- or overestimation of the core data. Dück et al. (2019) have shown that video imaging method for visualization of the freeze corer penetration into the sediment can bring a benefit in terms of quantification of shortening and is recommended to be used. In cases where the visibility at the benthic boundary layer is not good, the use of an echo-sounding technique for the measurement of the penetration depth is recommended.
4. Gravity coring is a relatively easy, cost-efficient method and requires less effort than freeze coring. It can, therefore, be used for the analysis of the vertical distribution of physical sediment parameter (e.g., GSD, WC, OM, and wet bulk density). This technique should only be sued for gas bubble analysis when the difference in hydrostatic pressure and temperature is small, to avoid related bias.

References

Abegg, F., and A. L. Anderson. 1997. The acoustic turbid layer in muddy sediments of Eckernfoerde Bay, Western Baltic: Methane concentration, saturation and bubble characteristics. Mar. Geol. **137**: 137–147. doi:10.1016/S0025-3227(96)00084-9

Acton, G. D., M. Okada, B. M. Clement, S. P. Lund, and T. Williams. 2002. Paleomagnetic overprints in ocean sediment cores and their relationship to shear deformation caused by piston coring. J. Geophys. Res. **107**: EPM 3-1-EPM 3-15. doi:10.1029/2001JB000518

Algar, C. K., B. P. Boudreau, and M. A. Barry. 2011. Initial rise of bubbles in cohesive sediments by a process of viscoelastic fracture. J. Geophys. Res. Solid Earth **116**: B04207. doi:10.1029/2010JB008133

Arman, A., and K. L. MacManis. 1976. Effects of storage and extrusion on sample properties, p. 66–87. In Symposium on soil specimen preparation for laboratory testing. ASTM STP: 599.

Bastviken, D., J. J. Cole, M. L. Pace, and M. C. Van de Bogert. 2008. Fate of methane from different lake habitats: Connecting whole-lake budgets and CH_4 emissions. J. Geophys. Res. **113**: G02024. doi:10.1029/2007JG000608

Bastviken, D., L. J. Tranvik, J. A. Downing, P. M. Crill, and A. Enrich-Prast. 2011. Freshwater methane emissions offset the continental carbon sink. Science **331**: 50–50. doi:10.1126/science.1196808

Baxter, M. S., J. G. Farmer, I. G. McKinley, D. S. Swan, and W. Jack. 1981. Evidence of the unsuitability of gravity coring for collecting sediment in pollution and sedimentation rate studies. Environ. Sci. Technol. **15**: 843–846. doi:10.1021/es00089a014

Blomqvist, S. 1985. Reliability of core sampling of soft bottom sediment - an in situ study. Sedimentology **32**: 605–612. doi:10.1111/j.1365-3091.1985.tb00474.x

Blomqvist, S. 1991. Quantitative sampling of soft-bottom sediments: Problems and solutions. Mar. Ecol. Prog. Ser. **72**: 295–304. doi:10.3354/meps072295

Boereboom, T., M. Depoorter, S. Coppens, and J.-L. Tison. 2012. Gas properties of winter lake ice in Norhtern Sweden: Implication for carbon gas release. Biogeosciences **9**: 827–838. doi:10.5194/bg-9-827-2012

Boudreau, B. P., et al. 2005. Bubble growth and rise in soft sediments. Geology **33**: 517–520. doi:10.1130/G21259.1

Buckley, D. E., W. G. MacKinnon, R. E. Cranston, and H. A. Christian. 1994. Problems with piston core sampling: Mechanical and geochemical diagnosis. Mar. Geol. **117**: 95–106. doi:10.1016/0025-3227(94)90008-6

Carte, A. E. 1961. Air bubbles in ice. Proc. Phys. Soc. **77**: 757–768. doi:10.1088/0370-1328/77/3/327

Chaney, R. C., and G. Almagor. 2015. Seafloor Processes and Geotechnology, 1st Edition. CRC Press. doi:10.1201/b19211

Chant, L. A., and R. J. Cornett. 1991. Smearing of gravity core profiles in soft sediments. Limnol. Oceanogr. **67**: 1492–1498. doi:10.4319/lo.1991.36.7.1492

Clayton, C. R. I., and A. Siddique. 1999. Tube sampling disturbance – forgotten truths and new perspectives. Geotech. Eng **137**: 127–135. doi:10.1680/gt.1999.370302

Crusius, J., and R. F. Anderson. 1991. Core compression and surficial sediment loss of lake sediment of high porosity caused by gravity coring. Limnol. Oceanogr. **36**: 1021–1031. doi:10.4319/lo.1991.36.5.1021

Duan, Z., N. Møller, J. Greenberg, and J. H. Weare. 1992. The prediction of methane solubility in natural waters to high ionic strength from 0 to 250°C and from 0 to 1600 bar. Geochim. Cosmochim. Acta **56**: 1451–1460. doi:10.1016/0016-7037(92)90215-5

Duc, N. T., P. Crill, and D. Bastviken. 2010. Implications of temperature and sediment characteristics on methane formation and oxidation in lake sediments. Biogeochemistry **100**: 185–196. doi:10.1007/s10533-010-9415-8

Dück, Y., L. Liu, A. Lorke, I. Ostrovsky, R. Katsman, and C. Jokiel. 2019. A novel freeze corer for characterization of methane bubbles and assessment of core disturbances. Limnol. Oceanogr.: Methods **17**: 305–319. doi:10.1002/lom3.10315

Elmgren, R. 1973. Methods of sampling sublittoral soft bottom meiofana. Oikos **15**: 112–120.

Emery, K. O., and R. S. Dietz. 1941. Gravity coring instrument and mechanics of sediment coring. Geol. Soc. Am. Bull. **53**: 1685–1714. doi:10.1130/GSAB-52-1685

Emery, K. O., and J. Hülsemann. 1964. Shortening of sediment cores collected in open-barrel gravity corers. Sedimentology **3**: 144–154. doi:10.1111/j.1365-3091.1964.tb00639.x

Environmental Protection Agency. 1991. Handbook: Remediation of contaminated sediments. EPA/625/6-91/028. Office of the Research and Development Washington DC 20460.

Flannagan, J. F. 1970. Efficiencies of various grabs and cores in sampling freshwater benthos. J. Fish. Res. Board Can. **27**: 1691–1700. doi:10.1139/f70-191

Flood, R. D., and others. 1995. Proceedings ODP, initial reports, 155: College Station, TX (Ocean Drilling Program). doi:10.2973/odp.proc.ir.155.1995

Förstner, U., G. Müller, and H.-E. Reineck. 1968. Sediment und Sedimentgefüge des Rheindeltas im Bodensee. Neues Jahrb. Min. Abh. **109**: 33–62.

Franchini, A. G., and J. Zeyer. 2012. Freeze-coring method for characterization of microbial community structure and function in wetland soilds at high spatial resolution. Appl. Environ. Microbiol. **78**: 4501–4504. doi:10.1128/AEM.00133-12

German Institute for Standardization (DIN)/International Organization of Standardization (ISO). 2016. Water quality - sampling – part 12: Guidance on sampling of bottom sediments (ISO/DIS 5667-12:2006).

Glew, J. R., J. P. Smol, and W. M. Last. 2001. Sediment Core Collection and Extrusion, p. 73–105. *In* Last W. M. and J. P. Smol [eds.], Tracking environmental change using lake sediments. Springer. doi:10.1007/0-306-47669-X_5

Grechishchev, S. E. 1972. Study results of thermal deformations and prediction of frost cracking of soils. *In* Proc. All-Union Sci. Conf. on Geocryology. Mosk. Gos. Univ.

Grechishchev, S. E. 1973. The basic regularities of thermogeology and temperature cracking of frozen soils. *In* Proc. 2nd Int. Conf. on Geocryology. Yakutsk. Kn. Izd.

Halde, R. 1980. Concentration of impurities by progressive freezing. Water Res. **14**: 575–580. doi:10.1016/0043-1354(80)90115-3

Harvey, B. R., M. B. Lovett, and S. J. Boggis. 1987. Some experiences in controlling contamination of environmental materials during sampling and processing for low-level actinide analysis. J. Radioanal. Nucl. Chem. **115**: 357–368. doi:10.1007/BF02037449

Hessler, R. R., and P. A. Jumars. 1974. Abyssal community analysis from replicate cores in the central North Pacific. Deep-Sea Res. Oceanogr. Abstr. **21**: 185–209. doi:10.1016/0011-7471(74)90058-8

Hongve, D., and A. H. Erlandsen. 1979. Shortening of surface sediment cores during sampling. Hydrobiologia **65**: 283–287. doi:10.1007/BF00038869

Hopper, R. J. 1992. Effects and implications of sampling clay soils. Ph.D. thesis. Univ. of Surrey.

Hung, W. T., W. H. Feng, I. H. Tsai, D. J. Lee, and S. G. Hong. 1997. Uni-directional freezing of waste activated sludges: Vertical freezing versus radial freezing. Water Res. **31**: 2219–2228. doi:10.1016/S0043-1354(97)00067-5

Hvorslev, M. J. 1949. Subsurface exploration and sampling of soils for civil engineering purposes. U. S. Army Corps of Engineers, Waterways Experimental Station.

Iovea, M., G. Oaie, O. G. Duliu, M. Bodale, G. Mateiasi, and M. Neagu. 2005. Single and dual-energy X-ray computer tomography and digital radiography study of sedimentary cores, p. 1337–1348. *In* Proceedings of the 7th International Conference on the Mediterranean Coastal Environment, October 25–29, Kusadesi, Turkey, MEDCOAST 2005.

Jensen, P. 1983. Meiofauna abundance and vertical zonation in a sublittoral soft bottom, with a test of the Haps corer. Mar. Biol. **74**: 319–326. doi:10.1007/BF00403458

Jutzeler, M., J. D. L. White, P. J. Talling, M. McCanta, S. Morgan, A. Le Friant, and O. Ishizuka. 2014. Coring disturbances in IODP piston cores with implications for offshore record of volcanic events and the Missoula megafloods. Geochem. Geophys. Geosyst. **15**: 3572–3590. doi:10.1002/2014GC005447

Kallstenius, T. 1958. Mechanical disturbances in clay samples taken with piston samplers. Royal Swedish Geotechnical Institute.

Kegwin, L., D. Rio, and G. D. Acton. 1998. Intermediate depth Blake outer ridge. Proc. Ocean Drill Prog. Init. Rep. **172**: 77–156. doi:10.2973/odp.proc.ir.172.104.1998

Ketcham, R. A., and W. D. Carlson. 2001. Acquisition, optimization and interpretation of x-ray computed tomographic imagery: Applications to the geosciences. Comput. Geosci. **27**: 381–400. doi:10.1016/S0098-3004(00)00116-3

Killawee, J. A., I. J. Fairchild, J. L. Tison, L. Janssens, and R. R. Lorrain. 1998. Segregation of solutes and gases in experimental freezing of dilute solutions: Implications for natural glacial systems. Geochim. Cosmochim. Acta **62**: 3637–3655. doi:10.1016/S0016-7037(98)00268-3

Lane, M. C., and K. H. Taffs. 2002. The LOG corer – a new device for obtaining short cores in soft lacustrine sediments. J. Paleolimnol. **27**: 145–150. doi:10.1023/A:1013547028068

Lebel, J., N. Silverberg, and B. Sundby. 1982. Gravity core shortening and pore water chemical gradients. Deep-Sea Res. **29**: 1365–1372. doi:10.1016/0198-0149(82)90014-0

Lee, D. J., and Y. H. Hsu. 1994. Fast freeze/thaw treatment on excess activated sludges: Floc structure and sludge dewaterability. Environ. Sci. Technol. **28**: 1444–1449. doi:10.1021/es00057a011

Leonard, R. 1990. An assessment of sediment loss and distortion at the top of short gravity cores. Sediment Geol. **66**: 57–63. doi:10.1016/0037-0738(90)90006-F

Li, L., J. Peng, Q. Gao, M. Sun, Y. Liu, M. Li, B. Chen, and K. Bo. 2016. Pressure retaining method based on phase change of coring of gas hydrate bearing sediments in offshore drilling. Appl. Therm. Eng. **107**: 633–641. doi:10.1016/j.applthermaleng.2016.06.174

Liernur, A., A. Schomburg, P. Turberg, C. Guenat, R.-C. Le Bayon, and P. Brunner. 2017. Coupling X-ray computed tomography and freeze-coring for the analysis of fine-grained low cohesive soils. Geoderma **308**: 171–186. doi:10.1016/j.geoderma.2017.08.010

Lipp, G., C. Körber, S. Englich, U. Hartmann, and G. Rau. 1987. Investigation of the behavior of dissolved gases during freezing. J. Cryobiol. **24**: 489–503. doi:10.1016/0011-2240(87)90053-8

Lisle, T. E. 1989. Sediment transport and resulting deposition in spawning gravels, north coastal California. Water Resour. Res. **25**: 1303–1319. doi:10.1029/WR025i006p01303

Liu, L., J. Wilkinson, K. Koca, C. Buchmann, and A. Lorke. 2016. The role of sediment structure in gas bubble storage and release. J. Geophys. Res. Biogeosci. **121**: 1992–2005. doi:10.1002/2016JG003456

Lotter, A. F., I. Renberg, H. Hansson, R. Stöckli, and M. Sturm. 1997. A remote controlled freeze corer for sampling unconsolidated surface sediments. Aquat. Sci. **59**: 295–303. doi:10.1007/BF02522360

Maeck, A., H. Hofmann, and A. Lorke. 2014. Pumping methane out of aquatic sediments: Ebullition forcing mechanisms in an impounded river. Biogeosciences **11**: 2925–2938. doi:10.5194/bg-11-2925-2014

Martens, C. S., and R. A. Berner. 1974. Methane production in the interstitial waters of sulfate-depleted marine sediments. Science **185**: 1167–1169. doi:10.1126/science.185.4157.1167

Martin, E. A., and R. J. Miller. 1982. A simple, diver-operated coring device for collecting undisturbed shallow cores. J. Sediment. Petrol. **52**: 641–642. doi:10.1306/212F7FC2-2B24-11D7-8648000102C1865D

McCoy, F. W., Jr. 1972. An analysis of piston coring through core head camera photography, p. 90–105. *In* E. D'Appolonia

[ed.], Underwater soil sampling, testing, and construction control. ASTM Spec. Tech. Publ. 501. ASTM International.

McCoy, F. W. 1980. Photographic analysis of coring. Mar. Geol. **38**: 263–282. doi:10.1016/0025-3227(80)90063-8

McCoy, F. W., and R.-P. von Herzen. 1971. Deep-sea core head camera photography and piston coring. Deep Sea Res. Oceanogr. Abstr. **18**: 361–373. doi:10.1016/0011-7471(71)90041-6

McIntyre, A. D. 1971. Deficiency of gravity cores for sampling meiobenthos and sediments. Nature **231**: 260. doi:10.1038/231260a0

Milkert, D. 1993. Auswirkungen von Stürmen auf die Sclicksedimente der westlichen Ostsee. Rep. Geol. Paläontol. Inst. Univ. Kiel **66**: 153.

Mogg, A. O., K. M. Attard, H. Stahl, T. Brand, R. Turnewitsch, and M. D. Sayer. 2017. The influence of coring method on the preservation of sedimentary and biogeochemical features when sampling soft-bottom, shallow coastal environments. Limnol. Oceanogr.: Methods **15**: 905–915. doi:10.1002/lom3.10211

Morton, R. A., and W. A. White. 1997. Characteristics of and corrections for core shortening in unconsolidated sediments. J. Coast. Res. **13**: 761–769.

Natchimuthu, S., I. Sundgren, M. Gålfalk, L. Klemedtsson, P. Crill, A. Danielsson, and D. Bastviken. 2016. Spatio-temporal variability of lake CH_4 fluxes and its influence on annual whole lake emission estimates. Limnol. Oceanogr. **61**: 13–26. doi:10.1002/lno.10222

Nevissi, A. E., G. J. Shott, and E. A. Crecelius. 1989. Comparison of two gravity coring devices for sedimentation rate measurement by ^{210}Pb dating techniques. Hydrobiologia **179**: 261–269. doi:10.1007/BF00006639

Nies, H., H. Albrecht, V. Rechenberg, I. Goroncy, H. Dahlgaard, D. Weiss, and L. Brugmann. 1990. Intercomparison of sediment sampling techniques by means of radionuclide and heavy metal analyses. Dt. hydrogr. Z. **43**: 27–53.

Ostrovsky, I. 2000. The upper-most layer of bottom sediments: Sampling and artifacts. Fundam. Appl. Limnol. Arch. Hydrobiol. **55**: 243–255.

Pachur, H. J., H. D. Denner, and H. Walter. 1984. A freezing device for sampling the sediment-water interface of lakes. Catena **11**: 65–70. doi:10.1016/S0341-8162(84)80006-5

Parker, P. J., A. G. Collins, and J. P. Dempsey. 1996. Incorporation and rejection of alum sludge flocs by an advancing freezing front, p. 757–767. *In* Proceedings of the 8th International Cold Regions Conference, August 12–16, Fairbanks, Alaska, United States.

Parker, W. R., and G. C. Sills. 1989. Observation of corer penetration and sample entry during gravity coring. Mar. Geophys. Res. **12**: 101–107. doi:10.1007/BF00310566

Piggot, C. S. 1941. Factors involved in submarine core sampling. Bull. Geol. Soc. Am. **52**: 1513–1523. doi:10.1130/GSAB-52-1513

Richards, A. F., and G. H. Keller. 1961. A plastic-barrel sediment corer. Deep-Sea Res. **8**: 306–312. doi:10.1016/0146-6313(61)90035-1

Rogasik, H., I. Onasch, J. Brunotte, D. Jegou, and O. Wendroth. 2003. Assessment of soil structure using X-ray computer tomography. Geol. Soc. Lond. Spec. Publ. **215**: 151–165. doi:10.1144/GSL.SP.2003.215.01.14

Rutledge, P. A., and J. W. Fleeger. 1988. Laboratory studies on core sampling with application to subtidal meiobenthos collection. Limnol. Oceanogr. **33**: 274–280. doi:10.4319/lo.1988.33.2.0274

Rymer, L., and J. Neale. 1981. Freeze coring as a method of collecting unconsolidated lake sediments. Aust. J. Ecol. **6**: 123–126. doi:10.1111/j.1442-9993.1981.tb01279.x

Scandella, B. P., C. Varadharajan, H. F. Hemond, C. Ruppel, and R. Juanes. 2011. A conduit dilation model of methane venting from lake sediments. Geophys. Res. Lett. **38**: L06408. doi:10.1029/2011GL046768

Schreiner, M., and K. Kreysing. 2013. Geotechnik hydrogeologie, 4th Edition. Springer.

Schubel, J. R. 1974. Gas bubbles and acoustically impenetrable, or turbid, character of some estuarine sediments. *In* I. R. Kaplan [ed.], Natural Gases in Marine Sediments. Plenum Press. doi:10.1007/978-1-4684-2757-8_16

Singh, K., and R. K. Niven. 2013. Non-aqueous phase liquid spills in freezing and thawing soils: Critical analysis of pore-scale processes. Crit. Rev. Environ. Sci. Technol. **43**: 551–597. doi:10.1080/10643389.2011.604264

Skinner, L. C., and I. N. McCave. 2003. Analysis and modelling of gravity- and piston coring based on soil mechanics. Mar. Geol. **199**: 181–204. doi:10.1016/S0025-3227(03)00127-0

Smith, D. G. 1992. Vibracoring: Recent innovations. J. Paleolimnol. **7**: 137–141. doi:10.1007/BF00196868

Smith, D. G. 1998. Vibracoring: A new method for coring deep lakes. Palaeogeogr. Palaeoclimatol. Palaeoecol. **140**: 433–440. doi:10.1016/S0031-0182(98)00031-5

Snider, L. J., B. R. Burnett, and R. R. Hessler. 1984. The composition and distribution of meiofauna and nanobiota in a central North Pacific deep-sea area. Deep-Sea Res. **31**: 1225–1249. doi:10.1016/0198-0149(84)90059-1

Stephenson, M., J. Klaverkamp, M. Motycka, C. L. Baron, and W. Schwartz. 1996. Coring artifacts and contaminant inventories in lake sediment. J. Paleolimnol. **15**: 99–106. doi:10.1007/BF00176992

Stowe, D. A. V., and A. E. Aksu. 1978. Disturbances in soft sediments due to piston coring. Mar. Geol. **28**: 135–144. doi:10.1016/0025-3227(78)90101-9

Strasser, D., H. J. Lensing, T. Nuber, D. Richter, S. Frank, N. Goeppert, and N. Goldscheider. 2015. Improved geohydraulic characterization of river bed sediments based on freeze-core sampling – development and evaluation of a new measurement approach. J. Hydrol. **527**: 133–141. doi:10.1016/j.jhydrol.2015.04.074

Sumer, B. M., and J. Fredsøe. 2002. The Mechanics of Scour in the Marine Environment. World Scientific. doi:10.1142/4942

Taft, R. A., and C. Jones. 2001. Sediment sampling guide and methodologies. State of Ohio Environmental Protection Agency.

Tsytovich, N. A. 1975. The mechanics of frozen ground. Scripta Book Company.

Varadharajan, C., and H. F. Hemond. 2012. Time series analysis of high resolution ebullition fluxes from a stratified, freshwater lake. J. Geophys. Res. Biogeosci. **117**: G02004. doi:10.1029/2011JG001866

Verschuren, D. 2000. Freeze coring soft sediments in tropical lakes. J. Paleolimnol. **24**: 361–365. doi:10.1023/A:1008191418497

Vesilind, P. A., and J. Martel. 1990. Freezing of water and wastewater sludges. J. Environ. Eng. **116**: 854–862. doi:10.1061/(ASCE)0733-9372(1990)116:5(854)

Wang, X. J., D. R. Hutchinson, S. G. Wu, S. X. Yang, and Y. G. Guo. 2011. Elevated gas hydrate saturation within silt and silty clay sediments in the Shenhu area, South China Sea. J. Geophys. Res. **116**: B05102. doi:10.1029/2010JB007944

Weaver, P. P. E., and P. J. Schultheiss. 1983. Direction of penetration and sediment disturbance in open-barrel gravity cores. J. Sediment. Petrol. **53**: 649–664. doi:10.1306/212F8256-2B24-11D7-8648000102C1865D

Wever, T. F., F. Abegg, H. M. Fiedler, G. Fechner, and I. H. Stender. 1998. Shallow gas in the muddy sediments of Eckernförde Bay, Germany. Cont. Shelf Res. **18**: 1715–1739. doi:10.1016/S0278-4343(98)00055-7

Wik, M., P. M. Crill, R. K. Varner, and D. Bastviken. 2013. Multiyear measurements of ebullitive methane flux from three subarctic lakes. J. Geophys. Res. Biogeosci. **118**: 1307–1321. doi:10.1002/jgrg.20103

Wilkinson, J., A. Maeck, Z. Alshboul, and A. Lorke. 2015. Continuous seasonal river ebullition measurements linked to sediment methane formation. Environ. Sci. Technol. **49**: 13121–13129. doi:10.1021/acs.est.5b01525

Wilkinson, J., P. Bodmer, and A. Lorke. 2019. Methane dynamics and thermal response in impoundments of the Rhine River, Germany. Sci. Total Environ. **659**: 1045–1057. doi:10.1016/j.scitotenv.2018.12.424

Wright, H. E., Jr. 1993. Core compression. Limnol. Oceanogr. **38**: 699–701. doi:10.4319/lo.1993.38.3.0699

Yvon-Durocher, G., and others. 2014. Methane fluxes show consistent temperature dependence across microbial to ecosystem scales. Nature **507**: 488–491. doi:10.1038/nature13164

Acknowledgments

The authors would like to thank Laura Bolsenkötter, Eric Zimmermann, and Timo Fahlenbock for their help throughout the sediment core sampling in the field. We would also like to thank Patrick Püttmann and Thomas Fortmeier for their help during laboratory experiment preparation. We thank Bettina Baeßler, Annika Thillmann, and Jasmin Holz for their assistance in X-ray CT scans. All data are provided in the Supporting Information. This study was conducted in the framework of a project of the European Regional Development Fund/Investment for Growth and Employment, project number EFRE-0800107.

Conflict of Interest

The authors declare no conflict of interest. The funding agency had no role in the design of the study; in the collection, analyses, or interpretation of data; in writing the manuscript; and in the decision to publish the results.

Submitted 30 March 2019
Revised 25 September 2019
Accepted 29 September 2019

Associate editor: George Waldbusser